WILEY | Hindawi

Research Article

A Novel Model-Based Adaptive Feedforward-Feedback Control Method for Real-Time Hybrid Simulation considering Additive Error Model

Xizhan Ning [iD],[1,2] **Wei Huang,**[1] **Guoshan Xu** [iD],[3] **Zhen Wang,**[4] **Bin Wu,**[4] **Lichang Zheng,**[3] **and Bin Xu** [iD][1,2]

[1]*College of Civil Engineering, Huaqiao University, Xiamen 361021, China*
[2]*Key Laboratory for Intelligent Infrastructure and Monitoring of Fujian Province, Huaqiao University, Xiamen 361021, China*
[3]*School of Civil Engineering, Harbin Institute of Technology, Harbin 150090, China*
[4]*School of Civil Engineering and Architecture, Wuhan University of Technology, Wuhan 430070, China*

Correspondence should be addressed to Guoshan Xu; xuguoshan@hit.edu.cn

Adaptive control methods have been widely adopted to handle the variable time delay in real-time hybrid simulation (RTHS). Nevertheless, the initial parameter settings in adaptive control law, the parameter estimation method, and the testing system nonlinearity will affect RTHS's accuracy and stability at different levels. To this end, this study proposes a novel model-based adaptive feedforward-feedback control method that considers an additive error model. In the proposed method, the time delay and amplitude discrepancy are roughly compensated by a feedforward controller and then finely reduced by an adaptive controller, and an outer-loop control formed by the feedback controller is introduced to improve the ability and robustness furthermore. What's more, the testing system, composed of the transfer system and physical specimen, is divided into the nominal and additive error models. The feedforward controller is devised using the inverse nominal model, whose parameters are constant. The adaptive controller is designed to adopt a discrete-time additive error model, in which the parameters are identified online by the Kalman filter. Numerical simulations, parametric studies, and actual experiments were carried out to inspect the feasibility and effectiveness of this method thoroughly. Results indicate that the proposed method can effectively improve the accuracy and stability of RTHS and significantly reduce the dependence on the adaptive control law. Moreover, the proposed method exhibits strong robustness and is, therefore, useful in RTHS.

1. Introduction

1.1. Background and Motivation. Real-time hybrid simulation (RTHS) [1] is a cost-effective and promising testing technique and has been extensively adopted for structural performance evaluation with rate-dependent behavior under dynamic excitation [2, 3]. In RTHS, the emulated structure is typically divided into two parts: the structural portion with a clear constitutive model is modeled numerically by a computer software, which is generally regarded as the numerical substructure (NS), and the remaining member exhibiting stronger nonlinearities is loaded physically and termed as physical substructure (PS). Nowadays, some new progresses have been made in RTHS considering structural or external excitation uncertainties [4–7]. In RTHS, the key issue is that displacement compatibility and force equilibrium on the boundary between NS and PS are enforced in real time [8–10].

Owing to the intrinsic dynamic of the transfer system (e.g., the servo-hydraulic actuator or shaking table), inevitable amplitude and phase errors exist between its accepted commanded and the actual response displacements. Moreover, the interaction between the actuator and PS [11], the data transition between the analog and digital signals,

and the noise in the experimental process can further increase the displacement desynchronization between the NS and PS. In addition, the abovementioned issues will lead to the desynchronization representing time-varying characteristics. Generally, this phenomenon is called time delay, which will reduce RTHS's accuracy and even cause instability problems [12–14]. Hence, the negative effect of time delay ought to be eliminated as much as possible.

In recent decades, various adaptive compensation/control methods have been proposed or improved to suppress RTHS's variable time delay. The classical control theory-based adaptive control schemes have been developed and widely used. For instance, an adaptive inverse compensation method was developed by Chen et al. [15] and its parameters were estimated and updated by the displacement tracking indicator. Chae et al. [16] advanced an adaptive time series compensator, designed by the input-output displacement time series relationship of the test system, and the compensator parameters are continuously updated by the least-squares method. Chen et al. [17] developed an adaptive model-based tracking controller using a parameter projection algorithm, and the stability was ensured by Routh's stability criteria. By combining model-based feedforward control and robust calibration of adaptive gains, Gálmez and Fermandois [18] proposed a robust adaptive model-based compensation framework. Najafi and Spencer [19] introduced a reference model and an adaptive law into the model-based feedforward-feedback control scheme to obtain high-precision RTHS results. Strano and Terzo [20] devised an adaptive control scheme, in which the control law was established by an inverse first-order transfer function and then updated online by the extended Kalman filter. Combining the frequency domain-based error indicators and the lead-lag controller, Mirza Hessabi et al. [21] designed a tracking error adaptive control method that exhibited the characteristics of high computational efficiency. Under the framework of feedforward and feedback control, Ning et al. [22] built a new adaptive control strategy using the discrete-time model of the physical testing system.

In contrast to the classical ones, the modern control theory-based adaptive control strategies have drawn much attention and proven to be more suitable for dealing with nonlinear testing systems. To improve the robustness and accuracy of the linear-quadratic-Gaussian (LQG) controller, Zhou et al. [23] developed a novel robust LQG controller using a loop transfer recovery procedure, and its tracking ability was validated by the benchmark problem of RTHS. The backstepping method was introduced by Ouyang et al. [24] to deal with variable time delay, and an adaptive control law was designed by Lyapunov stability analysis. To accomplish high performance and robust RTHS, Li et al. [25] established an adaptive sliding mode control method by combining the adaptive and robust control strategies. Aiming at enhancing RTHS's fidelity, Tsokanas et al. [4] introduced the adaptive strategy into the model predict control and designed a novel tracking controller.

Recently, adaptive strategies combining different control theories have been proposed and exhibited high control accuracy. For instance, Wang et al. [26] designed a two-stage adaptive control strategy, where the first stage was a polynomial extrapolation and the second stage was a discrete-inverse model-based adaptive delay compensator. Tao and Mercan [27] advanced an adaptive compensation scheme, in which the tracking error-based adaptive compensator was combined with a proportional-integral-derivative controller. Xu et al. [28] developed an adaptive combined compensation strategy using a sliding mode compensator and an improved adaptive forward prediction method to suppress time delay in RTHS. Combining the passivity control with an adaptive feedforward filter, Peiris et al. [29] developed a combined control method, with the advantages of low cost and the lower dependency on the prior knowledge about the test system.

Although the adaptive compensation methods have represented exceptional performance in literature, three main factors still affect their abilities. First, the adaptive method's performance depends profoundly on the initial setting of the model parameter. It requires explicit prior knowledge of the experimental testing system in general [17]. Second, the parameter estimation method plays a critical role in most adaptive compensation methods. A parameter estimation method with excellent ability ought to guarantee convergence, low dependency on the initial parameter setting, and high sensitivity to displacement tracking errors [30]. Third, the robustness is difficult to guarantee, especially for the complex nonlinear testing system [31].

1.2. Scope. In the field of robust control theory, the controller is generally established by using the nominal model of the control plant and its additive or multiplicative uncertainties, so as to ensure that the designed controller exhibits brilliant tracking capability and strong robustness in RHTS. On this basis, this study divides the control plant into a nominal model and an additive error model and establishes a novel model-based adaptive feedforward-feedback control method to solve the challenges in adaptive control methods. The proposed method comprises three parts: (1) a feedforward controller and (2) a discrete parametric adaptive controller to which a (3) feedback controller is added. In particular, the feedforward controller is designed by the control plant's inverse nominal model and its parameters are constant, and it can suppress the primary time delay and amplitude discrepancy. The adaptive controller is determined by a discretized additive error model, which can minimize the residual time delay. The feedback controller is introduced to enhance the robustness and further improve the control accuracy.

The main contents of this study are as follows. The background, the motivation, and the scope are introduced in Section 1. The formula of model-based adaptive feedforward-feedback control considering the additive error model will be introduced in Section 2. Then, Section 3 presents numerical validations, including the emulated structure and a nonlinear control plant, compensation strategies, tracking performance assessment, and parametric study. Subsequently, the experimental validations for the proposed method are demonstrated in Section 4, followed by the conclusions in Section 5.

2. Formula of Model-Based Adaptive Feedforward-Feedback Control Method

In this study, the control plant is composed of the transfer system and the PS. Its exact analytical model is often challenging to obtain, seriously affecting the design of the tracking controller. In robust control theory, the controller is generally designed based on the nominal model and the additive or multiplicative uncertainty of the control plant, and the robust controller has achieved excellent tracking performance [32]. Based on this, a novel adaptive model-based control scheme is conceived in this section.

2.1. Model-Based Feedforward Controller. In the proposed method, the control plant's analytical model is split into a nominal model G_0 and a corresponding additive error model G_Δ, as shown in Figure 1(a). When G_0 can commendably catch the control plant's dynamic characteristics, namely, G_Δ infinitely approaches 0, an excellent feedforward controller can be derived by the inverse of the nominal model, G_0^{-1}. As shown in Figure 1(a), the measured displacement d^m can match excellently the desired displacement d in this case.

However, the existence of uncertainties in PS and/or the transfer system can significantly weaken the effect of the feedforward controller. An additional control quantity d^a should be introduced to achieve outstanding tracking performance, as shown in Figure 1(b). In Figure 1, d^c denotes the commanded displacements, d^e is the error displacement produced from the additive error model G_Δ, d^0 denotes the displacement of the nominal model G_0, and d^{FF} represents the displacement generated by the inverse controller G_0^{-1}.

The form of the additional control quantity is derived as follows. The displacements d^c, d^m, and d^{FF} can be expressed as

$$d^c = d^a + d^{FF}, \tag{1}$$

$$d^m = (G_0 + G_\Delta)d^c, \tag{2}$$

$$d^{FF} = dG_0^{-1}. \tag{3}$$

Defining the tracking error e as

$$e = d - d^m, \tag{4}$$

then substituting (1)–(3) into (4), the tracking error e can be further expressed as

$$e = -G_0^{-1}G_\Delta d - (G_0 + G_\Delta)d^a. \tag{5}$$

In RTHS, the tracking error e is always expected to be 0, and then, the additional control quantity can be obtained, namely,

$$d^a = -\frac{1}{G_0}\frac{G_\Delta}{G_0 + G_\Delta}d. \tag{6}$$

However, the additional control quantity shown in (6) is usually very difficult to use due to the existence of G_Δ. It is necessary to simplify (6). Let $G_\Delta + G_0 = TG_0$, then (6) can be expressed as

$$d^a = -G_0^{-1}G_0^{-1}\frac{G_\Delta}{T}d, \tag{7}$$

where T is a frequency-dependent transfer function. The magnitude of T is almost 1 at the low frequency range and then gradually increases with the increase of frequency. In the field of earthquake engineering, the frequency of the structure and/or the earthquake excitation is generally very low, and one can always assume that the value of T is approximately 1, namely,

$$d^a = -G_0^{-1}G_0^{-1}G_\Delta d. \tag{8}$$

Thus, the model-based feedforward controller can be reached, as shown in Figure 1(c).

2.2. Real-Time Error Model Estimation. Typically, it is difficult to achieve the additive error model G_Δ in (8), because its amplitude is very small, especially in the low frequency range, say lower than 10 Hz, while, in the moderate frequency range, its amplitude increases gradually. The frequency response of the additive error model G_Δ exhibits differential or higher-order differential features, namely, the order of the numerator is higher than the denominator in the transfer function model. To facilitate practical use, this study adopts the discrete-time model of the additive error, and d_k^e at the kth time step can be expressed as

$$d_k^e = \sum_{j=1}^{q} x_j d_{k-j+1}^c, \tag{9}$$

where x is the additive error model parameter and q denotes the additive error model parameter number.

Because of the uncertainties in the control plant, the dynamic characteristics of the additive error model cannot be completely described by (9) with the given parameters. To address this issue, the error and commanded displacements are utilized to online estimate the additive error model G_Δ, which is denoted as $\hat{G}_\Delta$. It is assumed that the dynamics of the model error change slowly; thus, one can always treat the parameters in (9) as constants within a certain time span. Consequently, the problem of determining parameters in (9) belongs to a certain optimization or filter problem. While the least-squares method family is widely used, they are time-consuming concerning the calculation. Hence, considering the outstanding estimation performance, the Kalman filter (KF) algorithm is adopted in this study.

The state and measurement equations for estimating the additive error model can be expressed as

$$\begin{aligned} \mathbf{x}_{k+1} &= \mathbf{x}_k, \\ d_k^e &= \mathbf{H}_k^T \mathbf{x}_k + v_k, \end{aligned} \tag{10}$$

where $\mathbf{x}_k = [x_1, x_2, \cdots, x_q]^T$, $\mathbf{H}^T = [d_k^c, d_{k-1}^c, \cdots, d_{k-q+1}^c]$, and v_k is unknown zero mean white measurement noise with known covariance R.
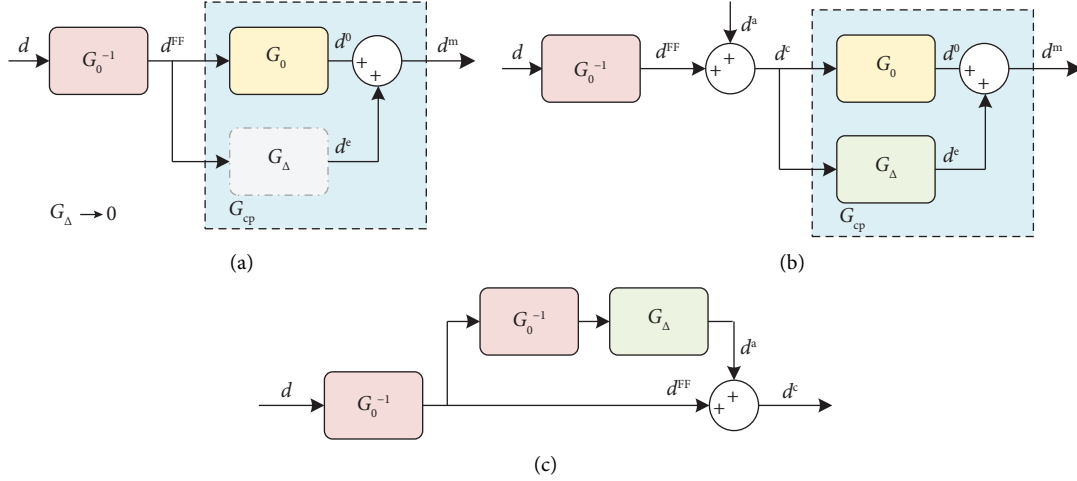
FIGURE 1: Schematic diagram of the additional control quantity. (a) Ideal case; (b) actual case; (c) feedforward controller.

The recursive estimation for the model parameters $\mathbf{x}_{k+1}$ can be expressed as

$$\hat{\mathbf{x}}_{k+1} = \hat{\mathbf{x}}_k + \mathbf{K}_k \left(d_k^e - \mathbf{H}_k^{\mathrm{T}} \hat{\mathbf{x}}_k \right), \tag{11}$$

in which $\mathbf{K}_k$ is the KF gain that is calculated by

$$\mathbf{K}_k = \mathbf{P}_{k-1} \mathbf{H}_k \left(\mathbf{H}_k^{\mathrm{T}} \mathbf{P}_{k-1} \mathbf{H}_k + R \right)^{-1}, \tag{12}$$

where $\mathbf{P}$ is the error covariance matrix of the state estimate, which is calculated by

$$\mathbf{P}_k = \left(\mathbf{I} - \mathbf{K}_k \mathbf{H}_k^{\mathrm{T}} \right) \mathbf{P}_{k-1}, \tag{13}$$

in which $\mathbf{I}$ is a unit matrix with respect to the dimension of the state vector $\mathbf{x}$.

Thus, the additional control quantity can be written as

$$d^a = -G_0^{-1} G_0^{-1} \widehat{G}_\Delta d \quad \text{or} \quad d_k^a = -\sum_{j-1}^{q} \hat{x}_j r_{k-j+1}, \tag{14}$$

where $\hat{x}$ denotes the estimate of the additive error model parameter and $r = -G_0^{-1} G_0^{-1} d$.

2.3. Feedback Controller.
A feedback controller is introduced to further enhance the robustness and improve the tracking performance. The proportional-integral (PI) controller is adopted in this study because of its facilitation, which can be expressed as

$$d_k^{\mathrm{FB}} = K_{\mathrm{P}} \xi_k + K_{\mathrm{I}} \sum \xi, \tag{15}$$

where d^{FB} is the displacement generated by the PI controller, K_{P} and K_{I} are the proportional and integral gains in the PI controller, respectively, and ξ denotes the difference between the desired displacement d and the measured displacement d^{m} that has been compensated for by the feedforward controller.

Thus, the formula of the model-based adaptive feedforward-feedback control method has been achieved, whose block diagram is shown in Figure 2. It is seen that the inverse model G_0^{-1} is served as the feedforward controller to eliminate the primary time delay in the control plant, and the adaptive controller is designed utilizing the additive error model to eliminate the residual time delay by online estimating the adaptive model parameters. Furthermore, the PI controller can increase the robustness and obtain a superior control performance.

3. Numerical Validation

The effectiveness and tracking performance for the proposed control strategy were accomplished and validated by two kinds of numerical simulations, including tracking performance assessment under prescribed displacements and a series of virtual RTHSs (vRTHSs). Considering that the testing system and PS will suffer different degrees of nonlinearity in an actual application, a nonlinear control plant, which comprises a nonlinear actuator model and a nonlinear specimen, is employed in this section.

3.1. Overview of the Simulation.
As shown in Figure 3, the emulated structure is a steel frame structure of three stories, and a magnetorheological (MR) damper is installed between the first floor and the ground floor. The steel frame structure is selected as the NS, while the MR damper is taken as the PS. Only the horizontal degrees of freedom (DOF) are considered for the NS. It is assumed that the mass is lumped at the floor levels and the mass for each floor is 2.05×10^4 kg. The lateral stiffness for each story is 3.773×10^7 N/m, and the calculated natural frequencies for each story are 3.04 Hz, 8.51 Hz, and 12.30 Hz, respectively. The structural damping matrix is calculated using the Rayleigh damping model, where the first two modal damping ratios are assumed to be 2%.

In the numerical simulations, the nonlinear actuator system model provided by Zhao et al. [33, 34] is employed to realize the displacement boundary coordination and force equilibrium between the two substructures, and its block diagram is revealed in Figure 4. As shown in the figure, the
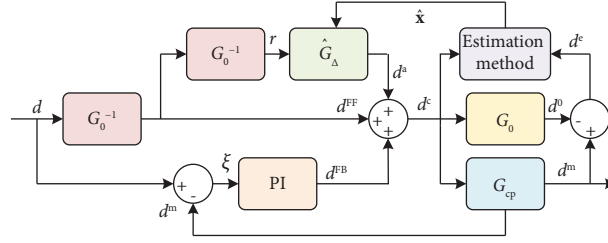
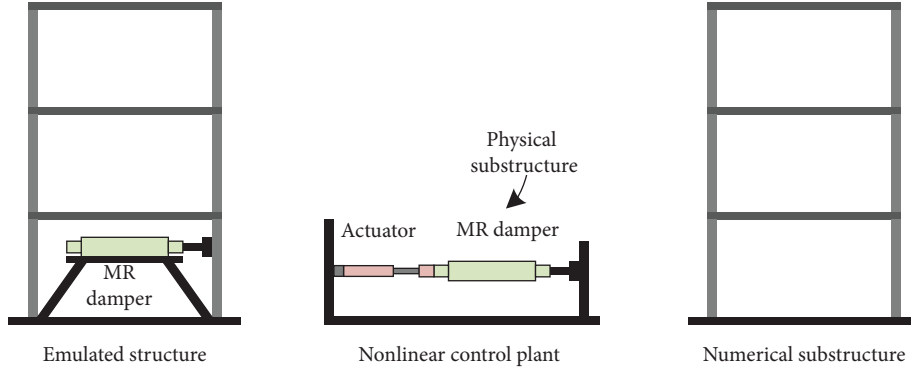FIGURE 2: Block diagram of the proposed method.

FIGURE 3: Emulated structure in the virtual RTHS.

nonlinear actuator model is mainly composed of an actuator and its servovalve, with the natural velocity feedback considered. The model can account for the effects of nonlinear factors in RHTS, including the flow property, response delay of the servovalve, and the interaction between the PS and the actuator. In addition, the Bouc–Wen model developed by Weber et al. [35] is used to represent the numerical model for the MR damper (Figure 4). The model is given by

$$
\begin{aligned}
f^{m}(i) &= \varsigma(i)E_v + \lambda(i)\dot{d}_{PS}, \\
E_v &= C\dot{d}_{PS} - \beta\dot{d}_{PS}|E_v|^n - \gamma|\dot{d}_{PS}|E_v|\dot{E}_v|^{n-1}, \\
\varsigma(i) &= \varsigma_a + \varsigma_b(i - 1.2i_{max})^2, \\
\lambda(i) &= \lambda_a + \lambda_b i,
\end{aligned}
\tag{16}
$$

where E_v is the evolutionary variable and $\varsigma(i)$ and $\lambda(i)$ are functions related to the input current i in the damper. The parameters and description of the servohydraulic actuator system and MR damper are shown in Tables 1 and 2, respectively.

3.2. Control Strategy.
As presented previously, the proposed adaptive control method incorporates a model-based feedforward-feedback strategy and a nominal model of the control plant should be identified first. Preliminary simulation with a duration of 60 s is performed using the uncontrolled control plant as stated previously, in which a 0.1~10 Hz swept signal owing an amplitude of 5 mm is served as the commanded displacement. To capture more

information from the control plant and to increase the reliability of the feedforward controller, a second-order transfer function without zeros is adopted to describe the dynamic of the nominal model, which could be expressed as

$$
G_{0,2} = \frac{9921}{s^2 + 201.6s + 9924},
\tag{17}
$$

where s represents the Laplace operator and the corresponding feedforward controller can be given in continuous time form in the time domain, namely,

$$
u_2 = 1.0080 \times 10^{-4}\ddot{t} + 0.0203\dot{t} + 1.0003t,
\tag{18}
$$

where t and u denote the input and output of the feedforward controller, respectively; the subscript "2" indicates that the inverse controller is second order.

A four-parameter difference equation is used to describe the additive error model and design the adaptive controller, which can be expressed as

$$
d_k^e = x_1 d_k^c + x_2 d_{k-1}^c + x_3 d_{k-2}^c + x_4 d_{k-3}^c.
\tag{19}
$$

Given the low nonlinearity of the control plant at the initial stage of the simulation, the model error between the nominal model and the control plant can be neglected. Hence, $\mathbf{x}_0$ can be expressed as $[0, 0, 0, 0]^T$, and $\mathbf{P}_0$ is represented by a fourth-order unit matrix. As for R, its value is 1×10^{-4} in this study.

Once the parameters are estimated, the additional control quantity d^a generated by the adaptive controller can be given by
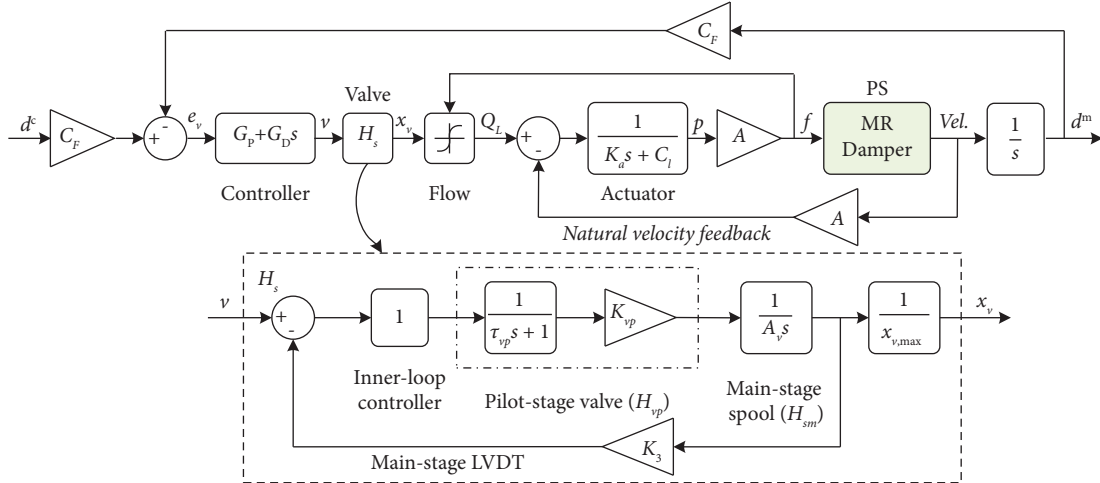
FIGURE 4: Nonlinear control plant model [33, 34].

TABLE 1: Parameter of the actuator [33, 34].

Item	Function	Value	Unit
C_F	Conversion factor	78.4	V/m
G_P	Proportional gain	3	—
G_D	Derivative gain	0	—
$x_{v\max}$	Maximum spool stroke	2.79×10^{-3}	m
K_{vp}	Valve flow gain	1.06×10^{-5}	m^3/s/V
τ_{vp}	Equivalent time constant	0.0014	s
A_v	Main-stage spool area	1.964×10^{-4}	m^2
K_3	Sensitivity factor	3579.13	V/m
K_v	Flow gain	1.64×10^{-2}	m^3/s
p_s	Pressure supply	1.9×10^4	kPa
C_l	Leakage coefficient	1.3×10^{-8}	m^3/s
K_a	Compressibility coefficient	7.56×10^{-10}	m^3/kPa
A	Actuator piston area	8.212×10^{-3}	m^2

TABLE 2: Parameter of the MR damper model [35].

Item	Function	Value	Unit
γ		200	m^{-1}
β	Parameters associated with the hysteretic loop	200	m^{-1}
n		2	—
C		5000	m^{-1}
ς_a	Shaping parameters	4250	N
ς_b		−27.78	N/A^2
λ_a	Parameters related to the viscous coefficient $c(i)$	1400	Ns/m
λ_b		1000	Ns/m/A

$$d_k^a = \widehat{x}_1 r_k + \widehat{x}_2 r_{k-1} + \widehat{x}_3 r_{k-2} + \widehat{x}_4 r_{k-3}. \tag{20}$$

As for the feedback controller, namely, the PI controller, K_P and K_I gains are set to 2 and 1, respectively. They were previously determined by the sinusoidal signal excited test, and the frequency and amplitude are 2 Hz and 5 mm, and the duration is 60 s.

This study also investigates the control strategy where the proposed method's feedback controller is removed, termed additive error model-based adaptive controller (AEM-AC). In addition, the inverse model (IM) control method is considered to demonstrate the necessity of introducing and estimating the error model online, which is given in (18).

3.3. Simulation Results and Analysis. The simulation results are evaluated from both qualitative and quantitative viewpoints. For the qualitative aspect, three indicators, namely, the calculated time delay J_1, the normalized roots mean square of the tracking error J_2, and the peak tracking error J_3, are used to evaluate the control performance. They are defined by

$$J_1 = \arg \operatorname*{Max}_{h} \left(\sum_k d_k d_{k-h}^{\mathrm{m}} \right),$$

$$J_2 = \sqrt{\frac{\sum_{k=1}^{\omega} \left(d_k - d_k^{\mathrm{m}} \right)^2}{\sum_{k=1}^{\omega} \left(d_k \right)^2}} \times 100\%, \qquad (21)$$

$$J_3 = \frac{\max \left| d_k - d_k^{\mathrm{m}} \right|}{\max \left| d_k \right|} \times 100\%,$$

in which ω is the number of displacement data points for d and d^{m}.

To assess the global performance of the virtual RTHS, six more indicators are employed, which are calculated by

$$J_{l+3} = \sqrt{\frac{\sum_{k=1}^{\omega} \left[\mathbf{D}_{\mathrm{R},k}^{(l)} - \mathbf{D}_{\mathrm{N},k}^{(l)} \right]^2}{\sum_{k=1}^{\omega} \left[\mathbf{D}_{\mathrm{R},k}^{(l)} \right]^2}} \times 100\ \%,$$

$$J_{l+6} = \frac{\max \left| \mathbf{D}_{\mathrm{R},k}^{(l)} - \mathbf{D}_{\mathrm{N},k}^{(l)} \right|}{\max \left| \mathbf{D}_{\mathrm{R},k}^{(l)} \right|} \times 100\ \%, \qquad (22)$$

where l denotes the lth floor of the emulated structure, J_{l+3} and J_{l+6} are the roots mean square error and the peak tracking error of the displacement for the lth floor, respectively, and $\mathbf{D}_{\mathrm{R}}$ and $\mathbf{D}_{\mathrm{N}}$ are the displacements measured from each story of the reference structure and numerical substructure, respectively. These nine evaluation indicators can also be found in Silva et al. [36].

3.3.1. Tracking Performance Assessment under Prescribed Displacement Command. Three earthquake displacement signals, named Dis.1, Dis.2, and Dis.3, respectively, are considered in this study, whose time histories are shown in Figure 5. They are obtained from the first-floor displacement responses of the Benchmark structures [36] excited by the El Centro, Kobe, and Morgan Hill seismic excitations (their peak ground accelerations (PGA) are all 0.4 g), respectively.

Figure 6 plots the displacement time histories (DTHs) of different control methods under three earthquake displacement signals, along with the enlarged views. It is seen from Figures 6(a), 6(c), and 6(e), and d^{m} greatly matches d on the whole, demonstrating the effectiveness of the three control strategies. The results in Figures 6(b), 6(d), and 6(f) show that there are evident amplitude and phase errors between the desired and measured displacements of the IM and AEM-AC methods for each prescribed displacement. Though the amplitude errors of IM and AEM-AC methods are comparable, the phase errors of AEM-AC are smaller

than those of IM, indicating the necessity of estimating the additive error model parameters online. The proposed method's measured displacement is almost identical to the desired displacements, illustrating its superior tracking ability. Comparing the results of the proposed and the AEM-AC methods demonstrates that the feedback controller is beneficial to improving the tracking performance.

The $J_1 \sim J_3$ values for different control methods under three earthquake displacement signals are plotted in Figure 7. The $J_1 \sim J_3$ values of AEM-AC are smaller than those of IM, implying that on the basis of the inverse model, adding to the additive error model and estimating its model parameters online can improve the control accuracy. When AEM-AC is compared with the proposed method, the J_1 and J_2 values of these two methods are nearly identical to each other. However, the J_3 values of the proposed method are smaller than those of AEM-AC, demonstrating that the feedback controller is attributed to remedy the displacement discrepancies at the peak further. The results indicate that the proposed controller exhibits strong robustness and brilliant tracking accuracy compared with the AEM-AC and IM methods.

Figure 8 presents the estimated time histories (ETHs) of the additive error model parameters under three earthquake displacement signals. The estimated error model parameters are broadly identical to each other. The estimated parameters start to update at the beginning of the simulation and then approach their corresponding constants at about the 5th second. The variation range of the estimated parameter for each earthquake displacement signal is relatively small. It could be attributed to the fact that the primary time delay is mainly suppressed by the feedforward controller, resulting in the smaller error displacement d^{e} and then the smaller estimated parameters. It could also be concluded from Figure 8 that the KF parameter estimation method can adjust the estimated parameters timely to drive the measured displacement tracking the desired displacement. Although the error displacements are tiny, the KF is sensitive enough to estimate the almost true parameters for the additive error model with high accuracy.

3.3.2. Results of the vRTHS. To better interpret the differences between the three control methods mentioned above, 15 vRTHSs for each control method are carried out and the results are presented in this section. Three different earthquake excitations are employed for each control method, namely, El Centro, Kobe, and Morgan Hill. The PGAs are scaled to 0.2 g, 0.3 g, 0.4 g, 0.5 g, and 0.6 g for each earthquake excitation.

The DTHs for three control methods under El Centro excitation with a PGA of 0.4 g are shown in Figure 9, with the enlarged views at zero and peak displacement at the same time provided. Figure 9(a) reveals a better agreement between the measured and desired displacements for different control strategies, whereas Figures 9(b) and 9(c) show notable differences in the amplitude and phase for IM and AEM-AC. The phase difference of AEM-AC is smaller than that of IM, while the amplitude discrepancy of AEM-AC is
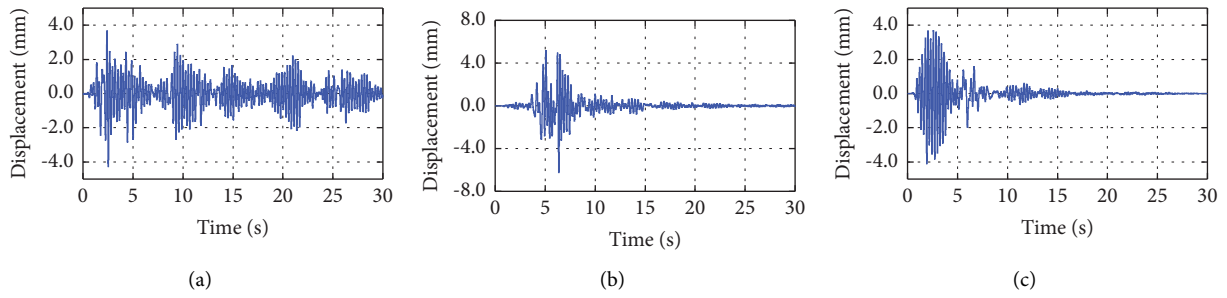
FIGURE 5: Earthquake displacement signals. (a) Dis.1; (b) Dis.2; (c) Dis.3.
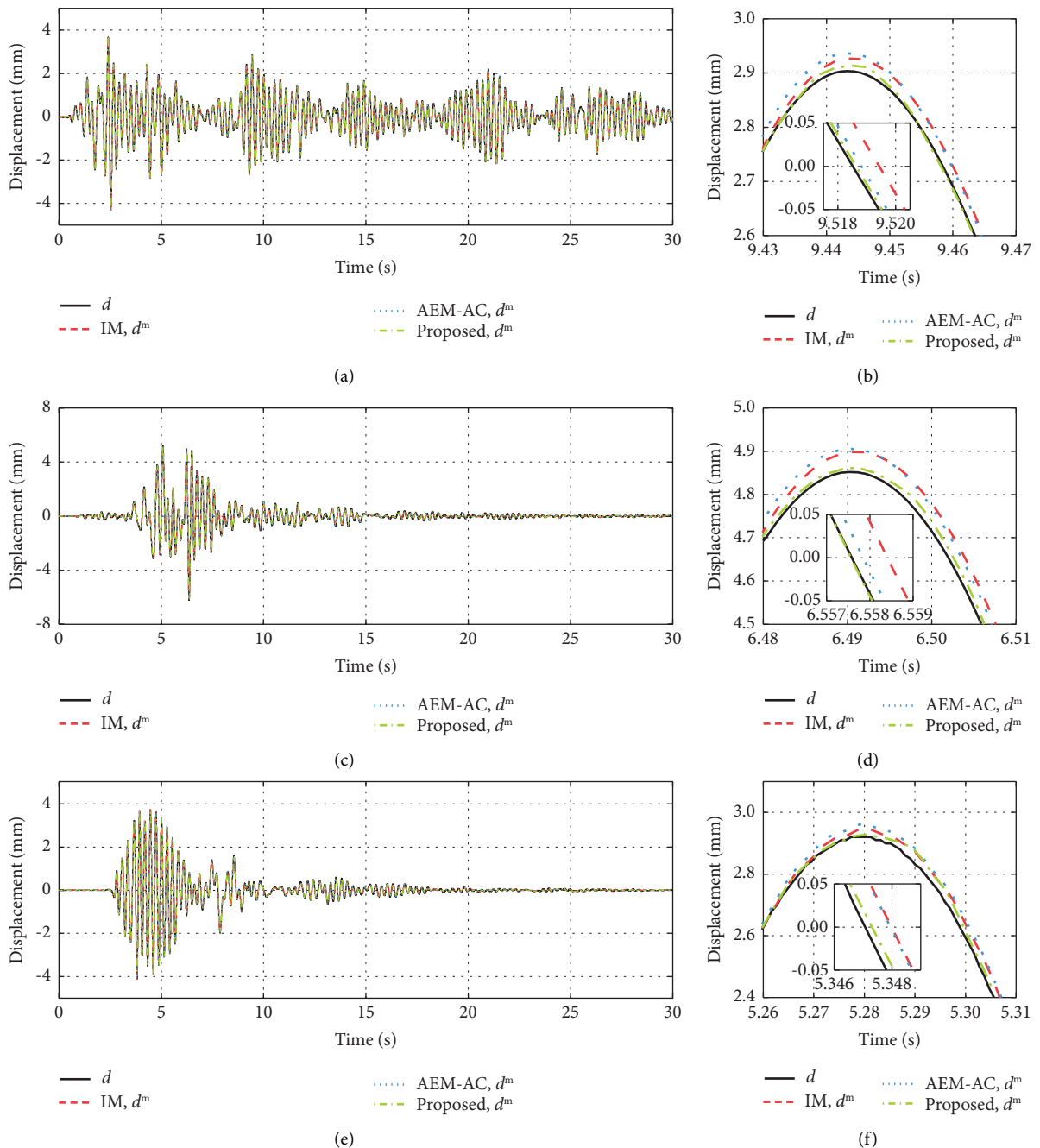

FIGURE 6: DTHs of three methods under prescribed displacements. (a) Global view of Dis.1; (b) enlarged view of (a); (c) global view of Dis.2; (d) enlarged view of (c); (e) global view of Dis.3; (f) enlarged view of (e).
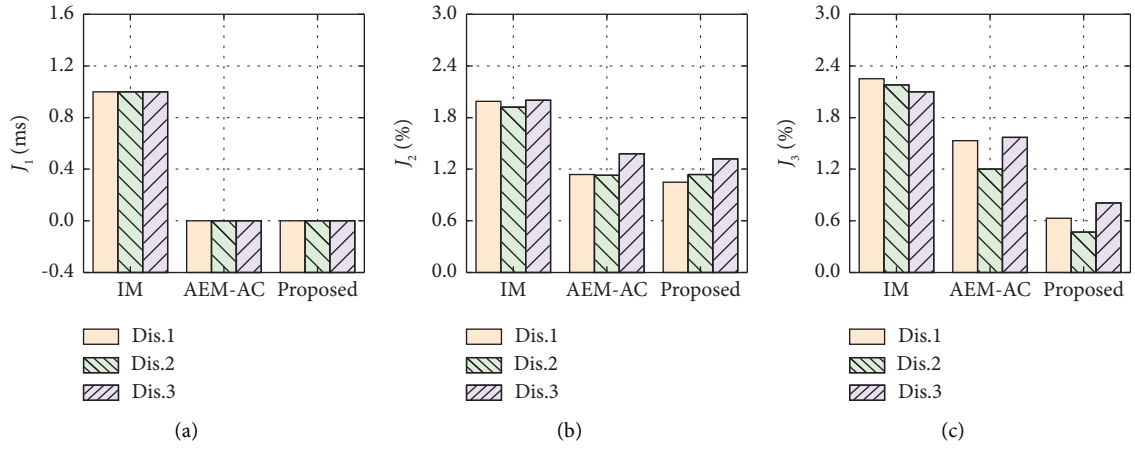
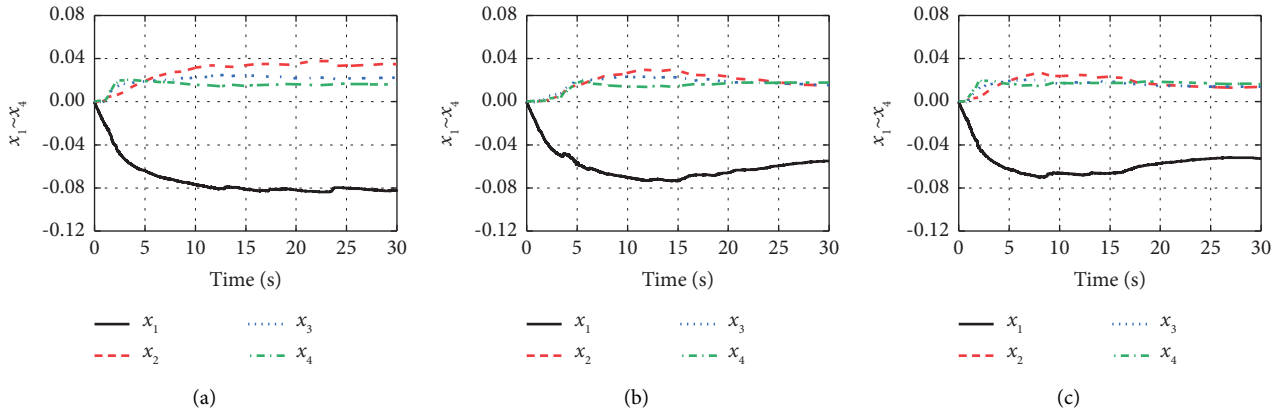FIGURE 7: $J_1 \sim J_3$ values under prescribed displacement. (a) J_1; (b) J_2; (c) J_3.

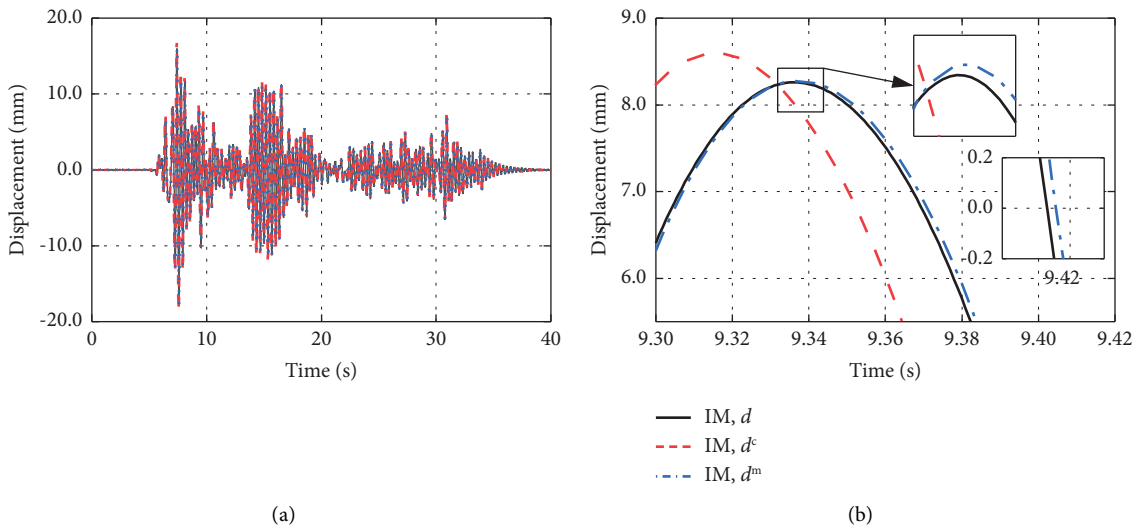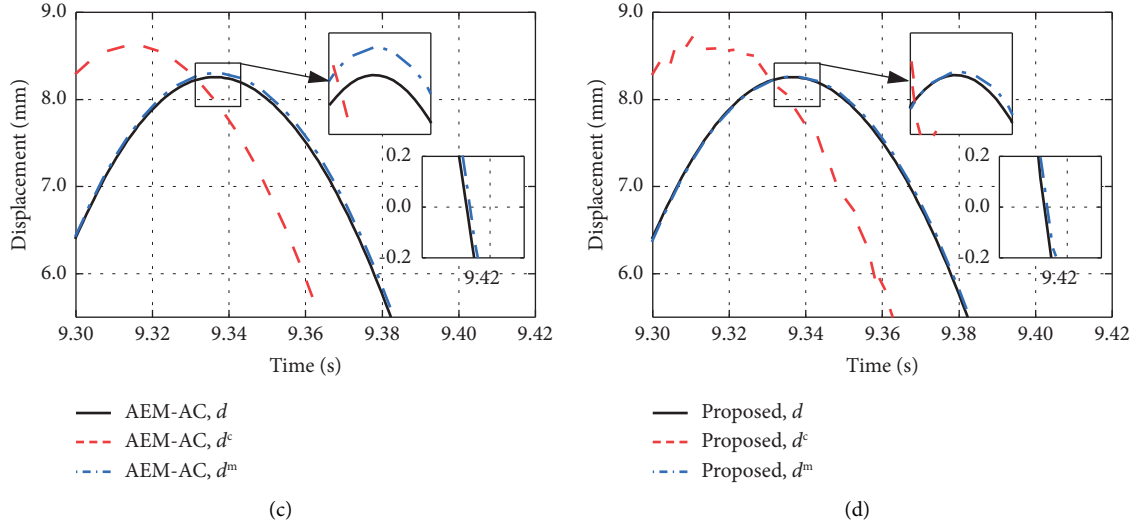FIGURE 8: ETHs of error model parameters. (a) Dis.1; (b) Dis.2; (c) Dis.3.

FIGURE 9: Continued.

(c)   (d)

FIGURE 9: DTHs for three control methods. (a) Global view; (b) enlarged view of the IM method; (c) enlarged view of the AEM-AC method; (d) enlarged view of the proposed method.

higher than that of IM. Figure 9(d) shows an excellent agreement between displacements d and d^{m}, demonstrating the superior performance of the proposed method.

To roundly compare the compensated ability of different control methods, Figure 10 gives the desired-measured (D-M) displacement plots under the considered three earthquake excitations with a PGA of 0.4 g. Here, the enlarged views of displacements d and d^{m} in the range of $[-1, 1]$ are also given. As shown in the figure, obvious hysteresis loops can be observed from the results of the IM method, while the AEM-AC method only exhibits slight hysteresis loops under three excitations. For the proposed method, D-M displacement plots are the thinnest, and the slope is almost equal to 1, implying an excellent tracking ability. This is consistent with the conclusions drawn from Figure 9.

The evaluation indicator values of the vRTHS are analyzed and plotted in Figure 11. The "Mean" and "STD" denote the mean and standard deviation of the evaluation indicator for the 15 vRTHSs of each control method, respectively. As shown in Figure 11, the "Mean" and "STD" of $J_1 \sim J_3$ values provided by IM are the largest among the three control methods, and they have been reduced significantly by AEM-AC, especially for J_1, whose "Mean" and "STD" both reduces to 0 ms. This demonstrates that it is essential to consider the additive error model. Focusing on the proposed method, it could be found that the "Mean" and "STD" of the above evaluation indicators are almost the smallest, indicating its superior tracking performance. It also implies that the feedback controller can improve the robustness of the proposed method. The proposed method has the smallest J_4 and J_7 values, either "Mean" or "STD." This indicates the proposed method exhibits an excellent fit between the reference and numerical results of the first floor. For the global performance of the second and third floors, the evaluation indicator values, namely J_5, J_6, J_8, and J_9, are almost identical to each other, implying the superior accuracy and robustness

of the two methods. In summary, the newly proposed model-based adaptive feedforward-feedback control method has supreme control performance in vRTHS.

Figure 12 describes the ETHs of the additive error model parameters for the proposed adaptive control method under three earthquake excitations with PGA scaled to 0.4 g. It shows that, the evolutions of the estimated parameters are almost identical to each other. In particular, the estimated parameters remain unchanged for the first 5 s because the small displacements and the nonlinearities are very weak. Then, the estimated parameters start to update, but they no longer converge to constant values. The reason could be that the displacements here are greater than those in Section 3.3.1, and the control plant comes into a strong nonlinearity. Nevertheless, the variation range of the identified parameters is relatively small for the three cases.

3.4. Parameter Study.
As described in Section 2, the control performance of the proposed method is mainly affected by the parameter estimation method, the inverse model order, and the additive error model parameter number. In order to investigate the influence of parameter settings in the proposed controller and provide guidance on controller design, a series of simulations are carried out using the control plant described in Figure 4 with the prescribed displacement commands as shown in Figure 5. Note that the values of the calculated time delay J_1 are 0 ms in the simulations, so they are not presented in this section.

3.4.1. Initial Settings in KF.
As presented in Section 2.2, the initial settings, namely, the initial state vector $\mathbf{x}_0$, the initial estimate error covariance matrix $\mathbf{P}_0$, and the measurement noise covariance R, play an important role in the KF method. Hence, we investigate their influences on the proposed method using the controller designed in Section
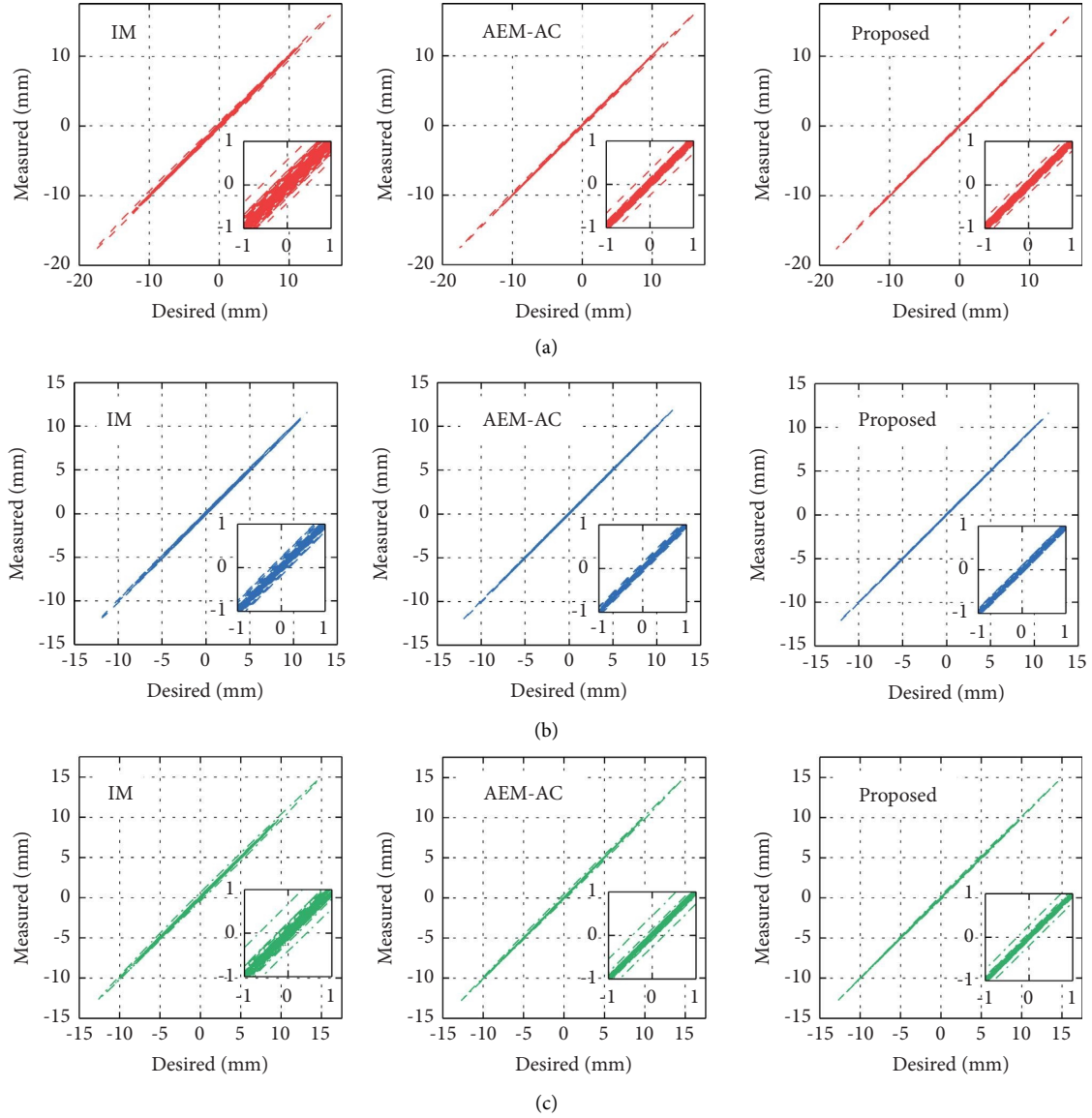
FIGURE 10: Desired-measured (D-M) displacement plots with a PGA of 0.4g. (a) El Centro; (b) Kobe; (c) Morgan Hill.

3.2. A parametric expression of the initial setting is adopted to represent their variation conveniently, which is defined as

$$B_f = Q_f B_0, \qquad (23)$$

where B_0 denotes the original initial settings $\mathbf{x}_0$, $\mathbf{P}_0$, and R, while B_f represents the variation of those parameters and Q_f is the variable factor, whose value is collected in Table 3.

A nonzero initial state vector is used in this section to fulfill the parameter analysis, which is calculated by the least-squares method utilizing the commanded displacement d^c and the error displacement d^e. The error displacement is determined by the difference between the second-order nominal model as shown in (17) and the nonlinear control plant. Thus, the initial state vector $\mathbf{x}_0$ used in (23) can be expressed by

$$\mathbf{x}_0 = [-0.0178, \ 0.0169, \ -0.0035, \ 0.0048]^{\mathrm{T}}, \qquad (24)$$

when $Q_f = 0$, the initial state vector calculated by (23) is identical to that used in Section 3.2.

Figure 13 plots the J_2 and J_3 values with different initial parameters under three prescribed displacements. The results in Figures 13(a) and 13(d) show that as Q_f becomes larger, the J_2 values almost remain unchanged for each described displacement, and the J_3 values also hold the same constant value under the Dis.3 command. In contrast, the J_3 values under Dis.1 and Dis.2 remain unchanged first and then become larger. Furthermore, the variation degree of J_3 under Dis.1 is higher than that under Dis.2. The J_3 value under Dis.1 begins to increase sharply when the value of Q_f is assigned to 14. At this time, the initial state vector is $[-0.2492, \ 0.2366, \ -0.0490, \ 0.0672]^{\mathrm{T}}$, which is a relatively

(a)

(b)

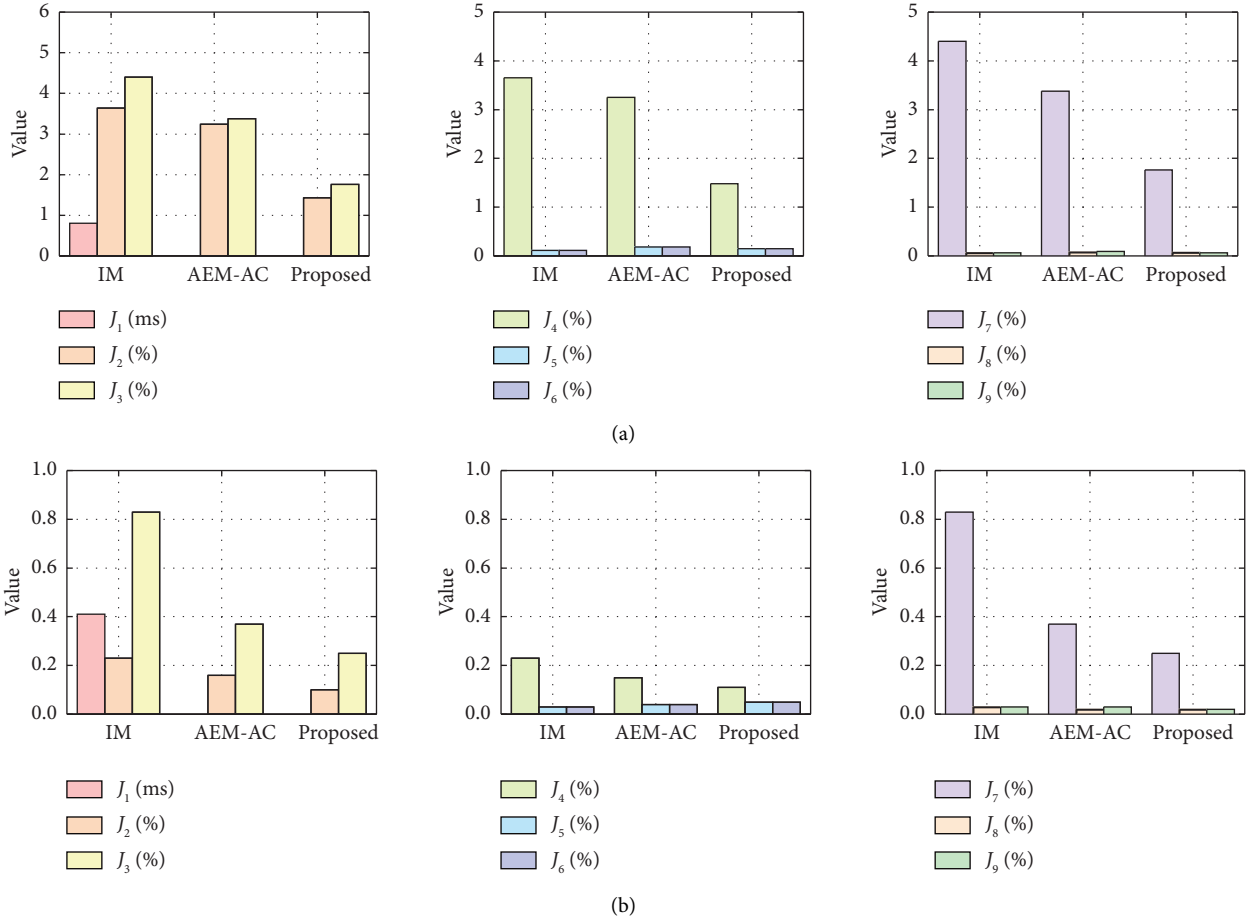Figure 11: Evaluation indicator of vRTHS. (a) Mean; (b) STD.

(a)   (b)   (c)
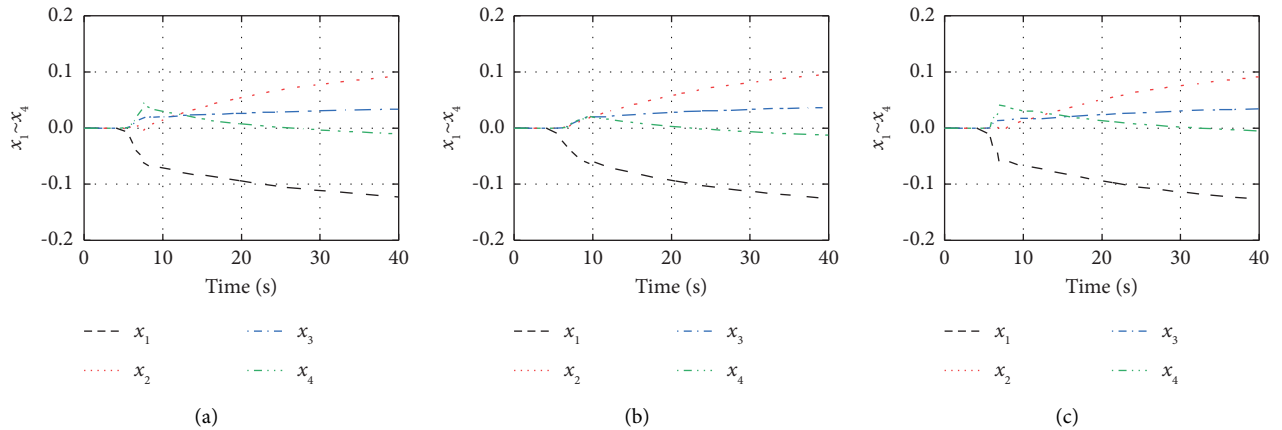
Figure 12: ETHs of the additive error model parameters. (a) El Centro; (b) Kobe; (c) Morgan Hill.

Table 3: Q_f settings for initial parameters.

Item	Range of Q_f	Increment
$\mathbf{x}_0$	0~20	2
$\mathbf{P}_0$	0.7~1.3	0.05
R	5~50	5

large value based on the results in Figures 8 and 12. Nevertheless, the J_3 values are still less than 4.5%. The results demonstrate that the initial state vector $\mathbf{x}_0$ has a limited influence on the proposed method's tracking performance and verify the rationality of setting the initial state vector $\mathbf{x}_0$ as a zero vector. Furthermore, the J_2 and J_3 values with
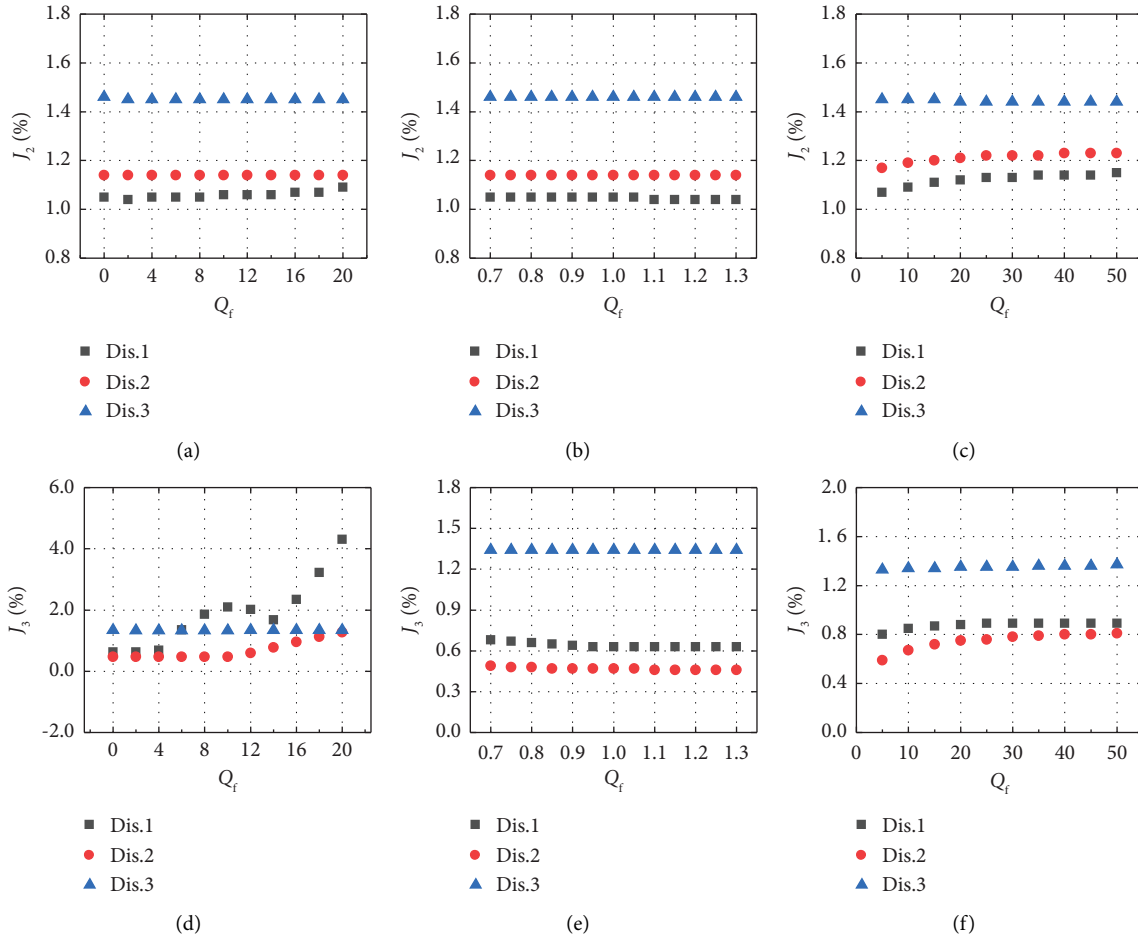
FIGURE 13: J_2 and J_3 values with different initial parameters. J_2 value with different (a) $\mathbf{x}_0$, (b) $\mathbf{P}_0$, and (c) R; J_3 value with different (d) $\mathbf{x}_0$, (e) $\mathbf{P}_0$, and (f) R.

different $\mathbf{P}_0$ or R almost remained for each prescribed displacement with Q_f becoming larger, as shown in the rest subgraphs from Figure 13. It indicates that the initial estimation error covariance matrix $\mathbf{P}_0$ and measurement noise covariance R have hardly any effect on the control ability of the proposed method.

3.4.2. The Inverse Model Order. To investigate the effect of the inverse model order on the control performance, four different inverse models, namely, first-, second-, third-, and fourth-order, are considered in this section. They are determined by their corresponding nominal models by the system identification for the nonlinear control plant using the same swept signal described in Section 3.2. The nominal and inverse models are listed in Table 4. Note that (19) is adopted to set up the additive error model.
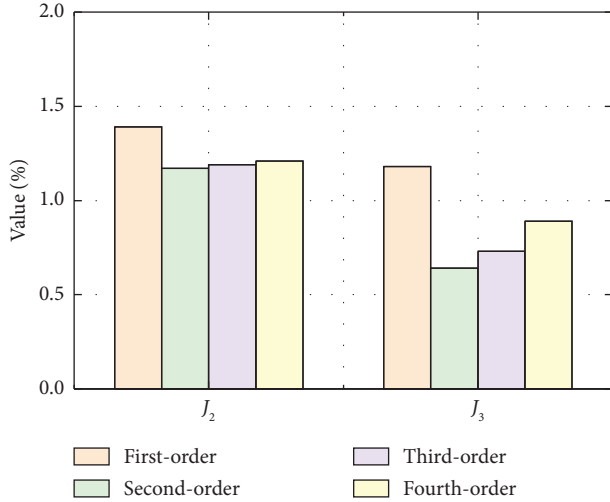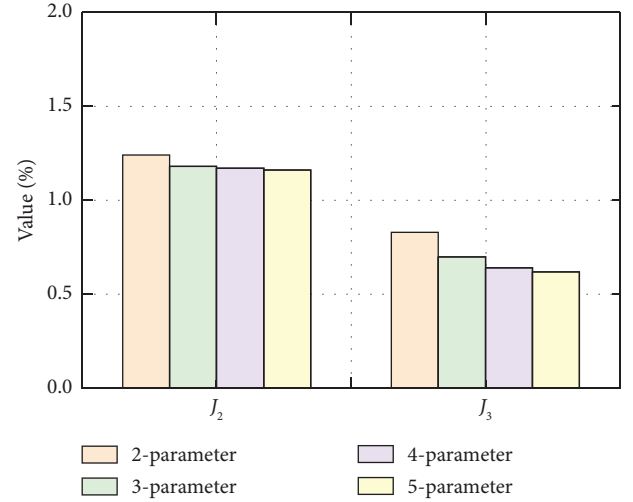
The J_2 and J_3 values with different inverse models are shown in Figure 14. These values represent the mean of J_2 and J_3 under the three prescribed displacements. The J_2 and J_3 values of the first-order inverse model are both the greatest. This is because the first-order nominal model is not accurate enough to represent the dynamic characteristics of the nonlinear control plant, leading to the poor control

accuracy of its corresponding feedforward controller. Theoretically, the fourth-order inverse model is the most suitable one for designing the feedforward controller, but its J_3 value is higher than those of the second- and third-order inverse models, although the differences in J_2 values of the three models are very small. The reasons may be interpreted as follows. The fourth-order inverse model can result in the lower error displacement d^e, in which the measurement noise may account for a large proportion. Thus, inaccurate additive model parameters may be estimated by the KF, resulting in poor control accuracy. Although the higher-order model may be conducive to fully reflecting the control plant's dynamic characteristics, it may adversely affect the control accuracy and complicate the control strategy design. Hence, the second- or third-order inverse model may be a candidate for the optimal model (Figure 14). Moreover, the first-order inverse model can also exhibit superior control accuracy if the low nonlinear of the control plant or permissible testing error is present.

3.4.3. Additive Error Model Parameter Number. This section investigates the influence of the additive error model parameter number. The simulation settings are as follows:

TABLE 4: Inverse and nominal models with different orders.

Order	Nominal model	Inverse model
1	$G_{0,1} = 48.66/(s + 45.36)$	$u_1 = 0.0206\dot{t} + 0.9322$
2	$G_{0,2} = 9921/(s^2 + 201.6s + 9924)$	$u_2 = 1.0080 \times 10^{-4}\ddot{t} + 0.0203\dot{t} + 1.0003$
3	$G_{0,3} = 7.584 \times 10^6/(s^3 + 763.7s^2 + 1.561 \times 10^5 s + 7.586 \times 10^6)$	$u_3 = 1.3186 \times 10^{-7}\dddot{t} + 1.0074 \times 10^{-4}\ddot{t} + 0.0206\dot{t} + 1.0003$
4	$G_{0,4} = 1.993 \times 10^{10}/(s^4 + 2628s^3 + 2.009 \times 10^6 s^2 + 4.1 \times 10^8 s + 1.993 \times 10^{10})$	$u_4 = 5.0176 \times 10^{-11}t^{(4)} + 1.3186 \times 10^{-7}\dddot{t} + 1.0080 \times 10^{-4}\ddot{t} + 0.0206\dot{t} + 1$

Figure 14: J_2 and J_3 values with different inverse models.

Figure 15: J_2 and J_3 values with different additive error models.

(i) the additive error model with 2-, 3-, 4-, and 5-parameter is considered; (ii) the nominal model and its corresponding feedforward controller are the same as shown in (17) and (18), respectively; (iii) the initial state vector $\mathbf{x}_0$ is set to zero vector considering its limited effect on the control performance; (iv) the initial estimation error covariance matrix $\mathbf{P}_0$ is set to a unit matrix, whose order is in accordance with the dimensions of $\mathbf{x}_0$; and (v) the value of measurement noise covariance R is the same as the setting presented in Section 3.2.

Similar to Figure 14, Figure 15 presents the mean values of J_2 and J_3 under three prescribed displacements with different additive error models. The values of J_2 and J_3 decrease slowly with the increase of parameter numbers for the additive error model. On the contrary, the variations of the evaluation indicator are very limited, demonstrating that the proposed method is robust to the additive error model parameter number. This is because the primary time delay has been largely eliminated, and the error displacements are relatively small, whose dynamics can be well modeled by a fewer-parameter-described time-varying model. Thus, increasing parameter numbers in the additive error model cannot improve the control accuracy. Despite the fact that the 5-parameter additive error model has the best control accuracy, it is not conducive to the control strategy design in real applications, because the estimated parameters in the higher-order model are more sensitive to the disturbances, leading to the estimated parameters with large fluctuations and then poor control accuracy. Therefore, considering the high-frequency dynamics and unclear nonlinear of the testing system, the additive model with a 3- or 4-parameter is sufficient to obtain superior control accuracy.

4. Experimental Verification of the Proposed Method

4.1. Experimental Setup and Structure Parameters.
In this section, actual RTHSs for demonstrating the feasibility and effectiveness of the proposed method were conducted on an energy dissipation structure at the Structural and Seismic Testing Center, Harbin Institute of Technology. As shown in Figure 16, the target structure was composed of a 4-story steel frame structure and a damper between the first floor and the ground floor. The frame structure was considered NS, and its dynamic model was simplified to a story shear model that only considers the horizontal degree of freedom. Each story's mass and lateral stiffness were assumed 20×10^3 kg and 5.9448×10^7 N/m, respectively. The damping ratios for the first two models were both set to 2%; thus, the calculated natural frequencies for each story were 3.01 Hz, 8.68 Hz, 13.29 Hz, and 16.31 Hz, respectively. The experimental installation, consisting of an MTS servohydraulic system, a damper, and a dSPACE real-time controller, is adopted to verify the proposed adaptive control method and compare its capacity with existing compensation/control methods. The MTS servoactuator can be capable of providing a maximum dynamic displacement of ±125 mm and a maximum force of 100 kN. As described in Figure 16, the damper was selected as the PS, which was in series with the actuator. The dSPACE controller was used for signal transition and test data acquisition and monitoring during RTHSs.

Similarly, with the earthquake input setting in vRTHS, three seismic excitations were employed, and the PGAs were scaled to 0.2 g, 0.3 g, 0.4 g, 0.5 g, and 0.6 g for each controller. In the actual RTHSs, the central difference method was utilized to solve the structural dynamic equation of the target structure, and the integration step was 1/1024 s.

4.2. Controller Design.
In the actual RTHS, besides the three control methods mentioned above, this study took into account the most widely used polynomial extrapolation (PE) method [37] and the recently developed Kalman filter-based adaptive delay compensation (KF-ADC) method [30]. The swept signal used in Section 3.2 was employed as the commanded displacement to identify the nominal and inverse models and to obtain the initial parameter settings of the KF-ADC method by the least-squares method.
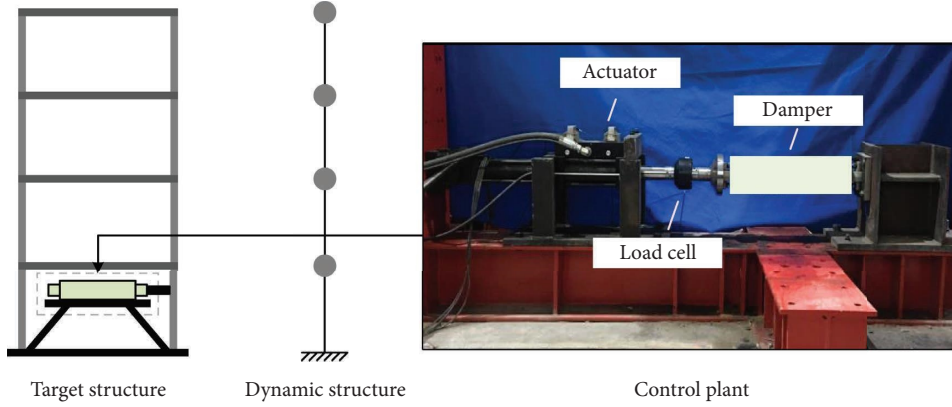
Figure 16: Target structure and substructure partition.

4.2.1. IM Method. Similar to the setting in Section 3.2, the nominal model was represented by a second-order transfer function given by

$$G_{0,2} = \frac{\theta_1}{s^2 + \theta_2 s + \theta_3}, \tag{25}$$

where $\theta_1 = 1.79 \times 10^4$, $\theta_2 = 187.4$, and $\theta_3 = 1.782 \times 10^4$. Considering the discreteness of the testing system, the IM method can be represented by the discrete-time form using the forward difference method. Thus, the corresponding inverse controller can be expressed as

$$u_{2,k} = \frac{1 + \theta_2 \Delta t + \theta_3 (\Delta t)^2}{\theta_1 (\Delta t)^2} t_k + \frac{-2 - \theta_2 \Delta t}{\theta_1 (\Delta t)^2} t_{k-1} + \frac{1}{\theta_1 (\Delta t)^2} t_{k-2}, \tag{26}$$

where Δt denotes the time interval between the adjacent displacement data points. In this study, the adjacent time interval was determined by every five displacement points, namely, $\Delta t = (5/1024)$ s, and this will reduce the adverse effects of measurement noise and ensure the smoothness of the displacement curve.

4.2.2. The Proposed and the AEM-AC Methods. The inverse model in the proposed and AEM-AC methods was the same as (26). For ease of use, the nominal model used to generate the error displacements was represented by a discrete transfer function.

$$G_{0,2}^{\text{dis}} = \frac{0.0080z + 0.0076}{z^2 - 1.817z + 0.8328}, \tag{27}$$

where z denotes the transformation operator.

   In addition, this study adopted the 4-parameter additive error model to set up the adaptive controller, whose parameter settings were the same as those used in Section 3.2.

   For the proposed method, the optimal PI gain was previously determined by a series of tests. These tests were all conducted for a duration of 60 s, adopting a 2 Hz sinusoidal signal owning 5 mm amplitude as the displacement input of the control plant. A total of 10 PI combinations were considered (Table 5), and the $J_1 \sim J_3$ values are shown in Figure 17. The results show that the PI gain has a limited

effect on the control performance. Combination 7, $K_P = 1.0$ and $K_I = 0.1$, is set to be the optimal PI gain for the proposed method because the J_3 value is the smallest in this case.

4.2.3. PE Method. The PE method is one of the most widely used methods for the time delay problem in RTHS because of its simple design and better compensation effect. This method utilizes three parameters to predict the displacement command of the next time step: the control plant's sampling frequency, the time delay, and the polynomial coefficients. Considering the influence of polynomial coefficients and the degree of nonlinearity in the control plant, this study used the 3-order PE method, which is expressed as

$$d_k^c = \left(\frac{1}{6}\eta^3 + \eta^2 + \frac{11}{6}\eta + 1\right)d_k - \left(\frac{1}{2}\eta^3 + \frac{5}{2}\eta^2 + 3\eta\right)d_{k-1}$$

$$+ \left(\frac{1}{2}\eta^3 + 2\eta^2 + \frac{3}{2}\eta\right)d_{k-2} - \left(\frac{1}{6}\eta^3 + \frac{1}{2}\eta^2 + \frac{1}{3}\eta\right)d_{k-3}, \tag{28}$$

where $\eta = \tau_{\text{De}}/\Delta t$ and τ_{De} is the calculated time delay. The displacement signal used in the PI gain determination was used to estimate the time delay offline, which was about 11.7 ms.

4.2.4. KF-ADC Method. In the KF-ADC method, the adaptive time-varying parametric compensator was developed by the discrete-time inverse model of the control plant and its coefficients were estimated online by the KF using d^c and d^m at each time step. In this study, the 4-parameter KF-ADC method was considered, which can be expressed as

$$d_k^c = \hat{\theta}_1 d_k + \hat{\theta}_2 d_{k-1} + \hat{\theta}_3 d_{k-2} + \hat{\theta}_4 d_{k-3}, \tag{29}$$

where $\hat{\theta}_1 \sim \hat{\theta}_4$ are the estimated model parameters at each time step. Their initial values were 2.4456, −2.7503, 2.1531, and −1.3700, respectively, which were calculated by the least-squares method. The initial estimation error covariance matrix was set to a 4-order diagonal matrix, whose diagonal elements are 2.4456^2, $(-2.7503)^2$, 2.1531^2, and $(-1.3700)^2$. The measurement noise covariance was the same as that used in Section 3.2.

TABLE 5: PI gain parameter settings for the proposed method in RTHS.

Combination	K_P	K_I
1		0
2	0.2	0.1
3		0
4	0.5	0.1
5		0.2
6		0
7		0.1
8	1.0	0.2
9		0.5
10	1.5	0
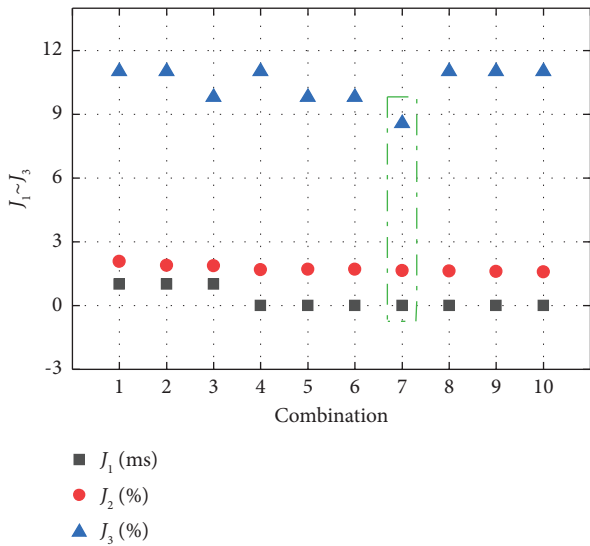
FIGURE 17: $J_1 \sim J_3$ of the proposed method with different PI gain combinations.

4.3. Assessment of Control Accuracy under Prescribed Displacement.

This section adopts five controllers designed in Section 4.2 to discuss the control accuracy of different control methods under prescribed displacement. Besides three earthquake displacement signals, a 0.1~5 Hz swept signal is also considered as the input of the control plant and the amplitude and duration are 5 mm and 100 s, respectively.

4.3.1. Earthquake Displacement Signal.

Figure 18 plots the DTHs of the considered methods under three earthquake displacement signals. Because of the great agreements between d^m and d, the global views are not given in this figure and only the enlarged views of the displacements around zero and peak at the same time are provided. For the IM and PE methods, there are significant differences in the agreement of both the phase and amplitude between the measured and desired displacements, indicating that the two methods exhibit poor displacement synchronization. Focusing on the enlarged view at around zero displacements, it can be concluded that the phase shift of the PE method is lower than that of the IM method, indicating that the PE method

has a better delay compensation ability. In addition, it can be seen that the KF-ADC method can significantly reduce both the phase shift and amplitude discrepancy and remarkably improve the synchronization between the measured and desired displacements. These facts demonstrate that the time delay is variable and can be effectively addressed by the KF-ADC method. Despite all this, there are still obvious displacement differences. Compared with PE, IM, and KF-ADC methods, the displacement d^m is in better agreement with the displacement d for the proposed and AEM-AC methods, indicating that the additional control quantity generated by the additive error model is beneficial for improving the tracking ability.

The mean values of $J_1 \sim J_3$ for different control methods under three earthquake displacement signals are plotted in Figure 19. It is seen that the IM method has the largest values of $J_1 \sim J_3$ and exhibits the worst compensation capability in all compared control methods. The values of $J_1 \sim J_3$ for the PE method are improved slightly compared to those of the IM method. Though the J_3 values of PE and KF-ADC are roughly the same, the J_1 and J_2 values of the latter are significantly reduced, demonstrating the greater time delay compensation accuracy of the KF-ADC method. The J_1 values of the AEM-AC and proposed methods are both 1 ms, but the J_2 and J_3 values of the proposed method are smaller. In general, error indicators of the proposed method are the smallest, implying that considering the modeling errors can significantly improve the tracking ability and the feedback control is conducive to promoting the control accuracy.

4.3.2. Swept Signal.

Figure 20 provides the absolute tracking error (ATE), i.e., the absolute error between displacements d and d^m at each time step. This study also calculated and plotted the maximum and mean values of the tracking errors, denoted by "Max" and "Mean," respectively. Figure 20 demonstrates that the distribution ranges of the ATE for the proposed and the AEM-AC methods are smaller than those for IM, PE, and KF-ADC methods. The tracking errors for IM, PE, and KF-ADC methods rise as time goes on, while for the proposed and the AEM-AC methods, the tracking errors increase gradually at the first 20 s and then decrease progressively and reach the lowest values at around 85 s. As shown in Figures 20(a)~20(c), both the "Max" and "Mean" of the IM method are the greatest, followed by the PE method. In contrast to the above two methods, the KF-ADC method shows a better control ability. However, the tracking error for the KF-ADC method has a spike point of about 0.2 mm at 0 s (marked by a green point in Figure 20(c)). Figures 20(d) and 20(e) show that the "Max" and "Mean" of the tracking error are identical in the proposed and the AEM-AC methods and are both significantly lower compared with the other three methods. The results demonstrate that the proposed and the AEM-AC methods exhibit excellent control performance.

The obtained $J_1 \sim J_3$ values with different methods are plotted in Figure 21. It is seen that the IM method performs the worst, followed by the PE and KF-ADC methods. The $J_1 \sim J_3$ values are nearly identical for the proposed and the
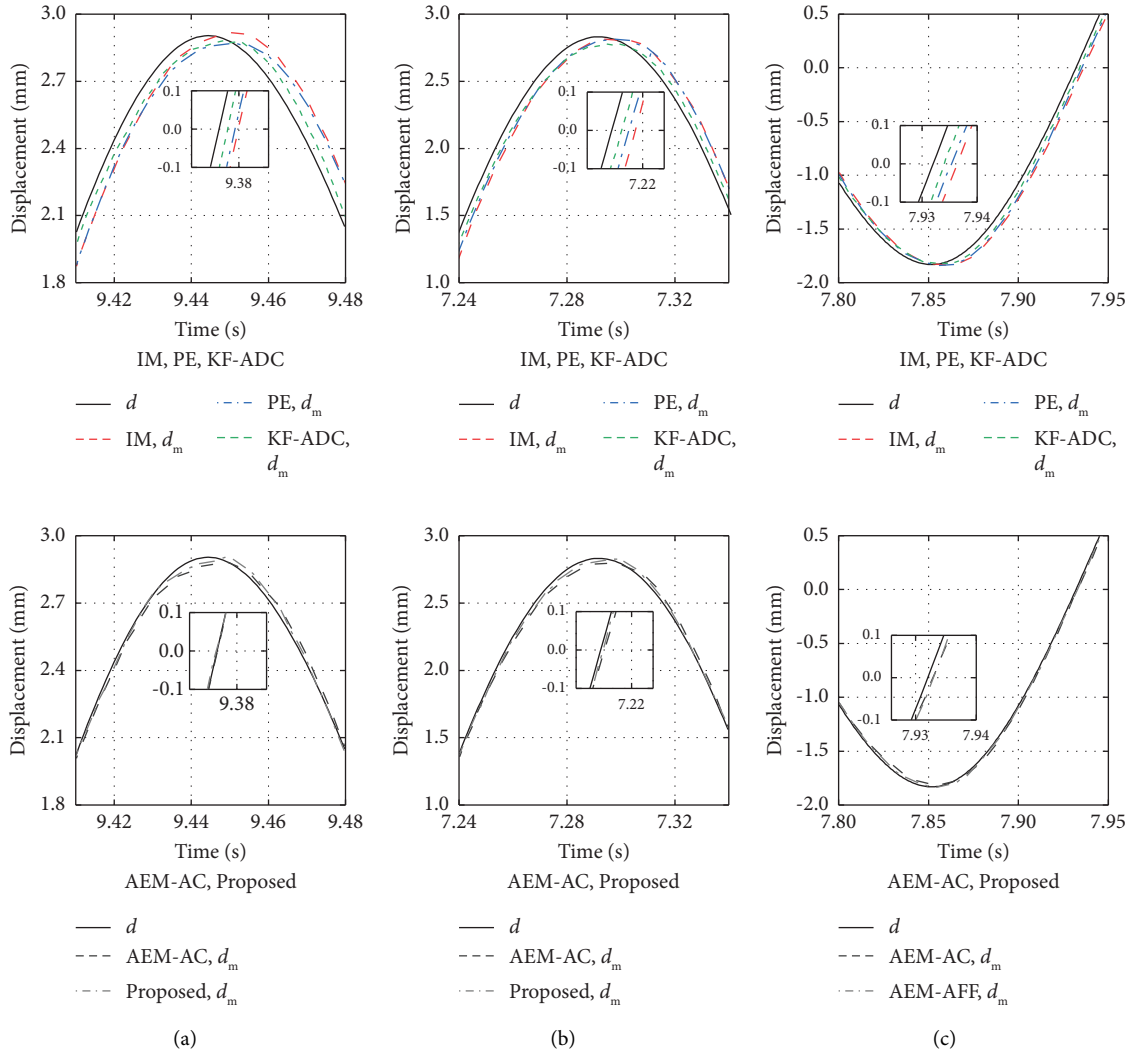
FIGURE 18: Enlarged view of DTHs for different control methods under three earthquake displacement signals. (a) Dis.1; (b) Dis.2; (c) Dis.3.
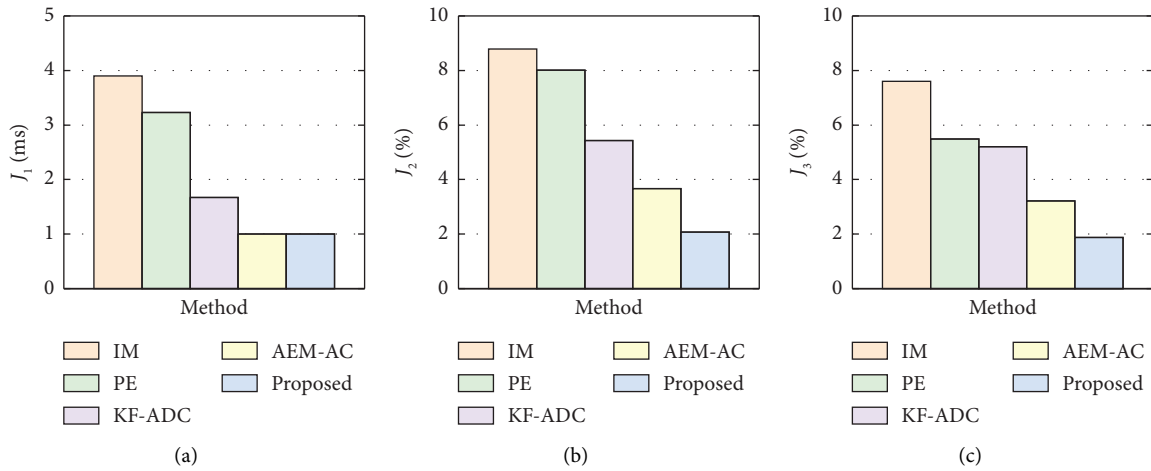

FIGURE 19: $J_1 \sim J_3$ for different control methods under earthquake displacement signal. (a) J_1; (b) J_2; (c) J_3.
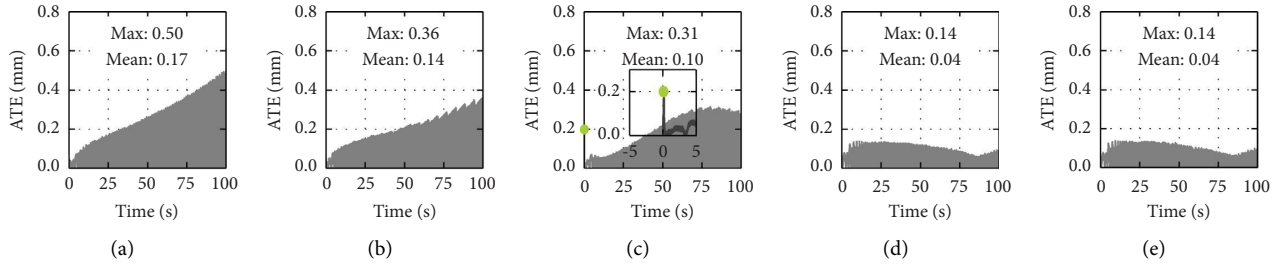
FIGURE 20: Time histories of ATE for different methods under swept signal. (a) IM method; (b) PE method; (c) KF-ADC method; (d) AEM-AC method; (e) proposed method.

AEM-AC methods, and they are the smallest in all the comparative methods. In particular, the calculated time delay J_1 values in these methods are reduced to 0 ms.

Figure 22 gives the ETHs of the additive error model parameters for the proposed method. The error model parameters are updated immediately as soon as the test begins and has a fast change speed in the first 20 s. Afterward, the estimated parameters gradually change. Although the estimated parameters do not converge to constant values, they fluctuate within a very limited range. The main reason for this fact is that, under the swept signal, the control plant was negatively affected by different nonlinearities and the increasing frequency of the signal, resulting in a significant variation in time delay. To track the commanded displacement, the control plant parameters must be adjusted correspondingly.

4.4. Results of RTHS. Figure 23 plots the DTHs of the considered methods under El Centro excitation with a PGA of 0.4 g, where the enlarged views of the displacement around zero and peak displacement at the same time are also provided. The measured displacements with different control methods match the desired displacements very well on the whole, as shown in Figure 23(a). However, there are profound differences among different control methods if focusing on the enlarged view. As depicted in Figures 23(b)~23(d), there are very large amplitude discrepancies and phased shifts for IM and PE methods, while the KF-ADC methods effectively improve these. However, poor agreements between the desired and measured displacements also exist at peak displacement for the KF-ADC method. As presented in Figures 23(e) and 23(f), amplitude discrepancies or phase shifts can hardly be recognized from the DTHs of the proposed and the AEM-AC methods. Furthermore, the proposed method yields a perfect agreement between the measured and desired displacements, regardless of zero or peak displacement. The results indicate that the model-based adaptive feedforward-feedback control method has the best displacement fit and exhibits excellent control accuracy in RTHS among the considered control methods.

Figure 24 plots the hysteresis relationships of the damper in the RTHS under three seismic excitations with PGAs scaled to 0.4 g. It is seen in the figure that the force increases with the growth of displacement in the positive direction, whereas the force measured from the damper is almost zero

in the negative displacement range, demonstrating the damper suffers strong nonlinearity. In particular, the hysteresis relationship curves under El Centro and Morgan Hill are fatter than those under Kobe, demonstrating that the damper in RTHS suffered a stronger nonlinearity under the former earthquake excitations.

The D-M displacement plots of different control methods under the considered three excitations with a PGA of 0.4 g are shown in Figures 25(a)~25(c), respectively. As presented in the figure, hysteresis loops can be detected for the IM and PE methods, while this phenomenon is effectively improved for the KF-ADC and AEM-AC methods. However, displacements d and d^m cannot still perfectly anastomose in the D-M displacement plots for the KF-ADC method. For the proposed method, its D-M displacement plot is the thinnest, which is approximated as a straight line with a slope of 1.

Figure 26 plots the $J_1~J_3$ values of the considered control methods in RTHS. In the figure, the implications of "Mean" and "STD" are the same as the descriptions in Figure 11. The results in Figure 26(a) show that the "Mean" value of $J_1~J_3$ for the IM method is the greatest, followed by the PE method, and the proposed method is the smallest, indicating the perfect tracking performance of the proposed method and the necessity of adaptive control strategy. Compared with the IM method, the "Mean" values of $J_1~J_3$ for the AEM-AC method shrank by more than 50%, indicating that the tracking performance can be improved by considering the additive error of the control plant. Moreover, the "STD" values of J_1 for the five methods are shown to be nearly identical to each other in Figure 26(b), while the proposed method has the lowest "STD" value for J_2 and J_3. It demonstrates that the proposed method exhibits stronger robustness.

A comparison of the three adaptive control schemes shows that the KF-ADC method has the worst control accuracy, whereas the proposed and the AEM-AC methods can more effectively solve the variable time delay problem in RTHS. The reason may be attributed to the following facts. The KF-ADC method cannot deal with the relatively high-frequency dynamics of the system, resulting in the accumulation of test errors, and the unreasonable initial parameter settings can further reduce its control accuracy. For the proposed and the AEM-AC methods, the feedforward controller largely eliminates the primary time delay, and the time-variant additive error model is conducive to
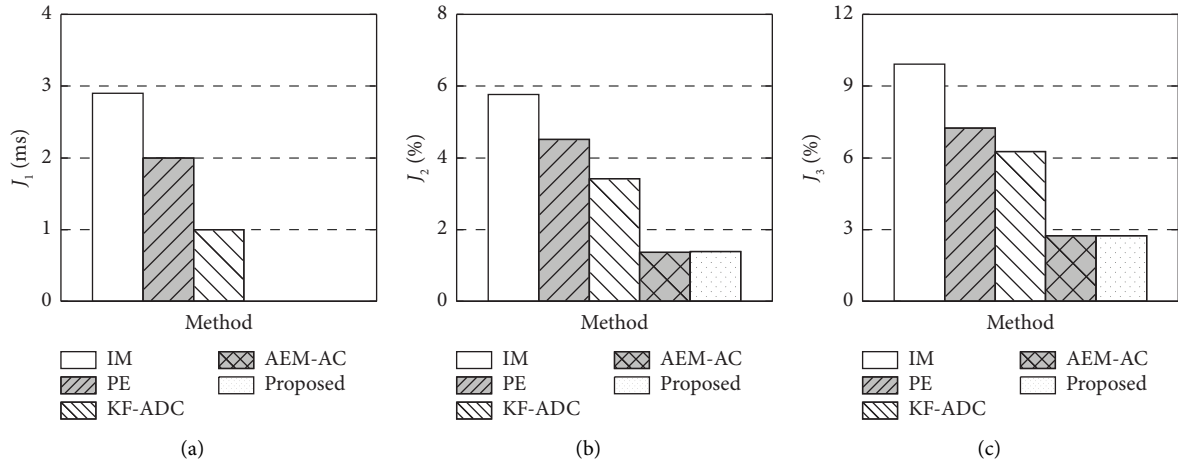
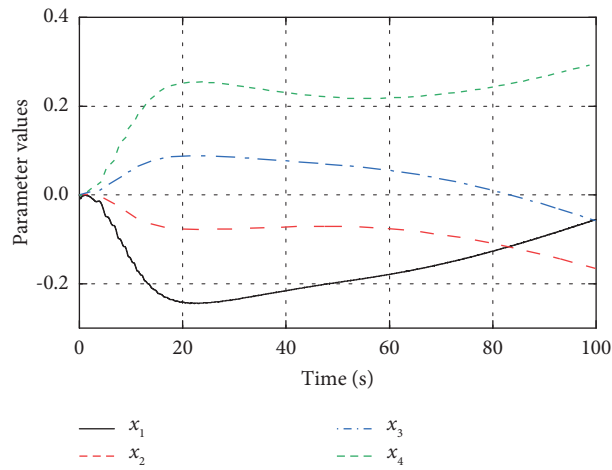Figure 21: $J_1 \sim J_3$ of the different methods under swept signal. (a) J_1; (b) J_2; (c) J_3.

Figure 22: ETHs of the additive error model parameters under swept signal.

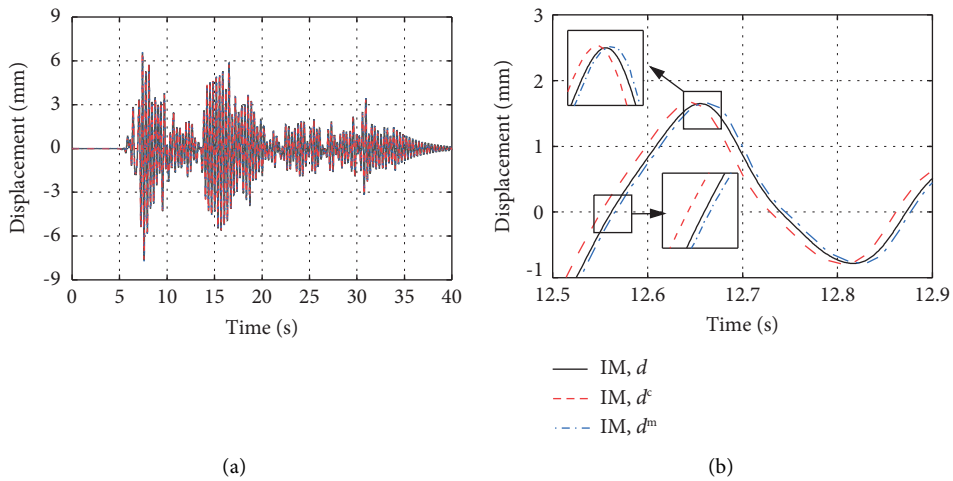(a)   (b)
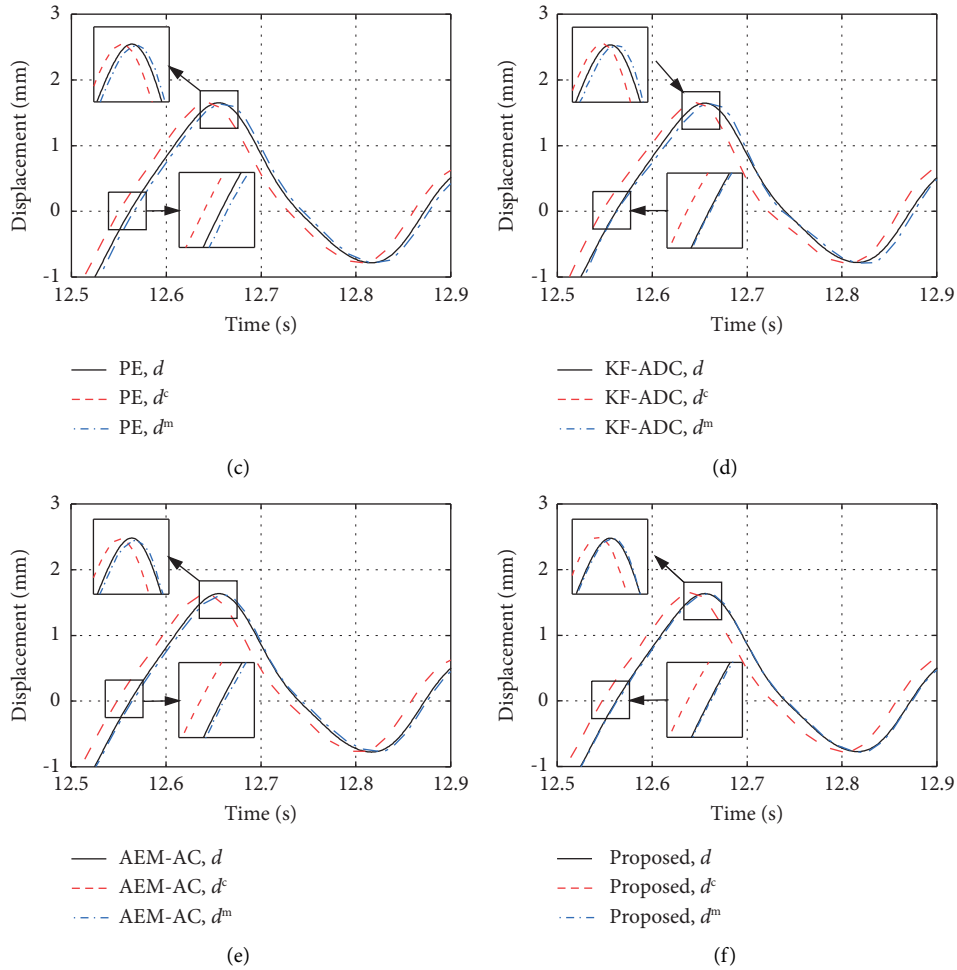
Figure 23: Continued.

Figure 23: DTHs of comparative methods. (a) Global view; (b) enlarged view for the IM method; (c) enlarged view for the PE method; (d) enlarged view for the KF-ADC method; (e) enlarged view for the AEM-AC method; (f) enlarged view for the proposed method.
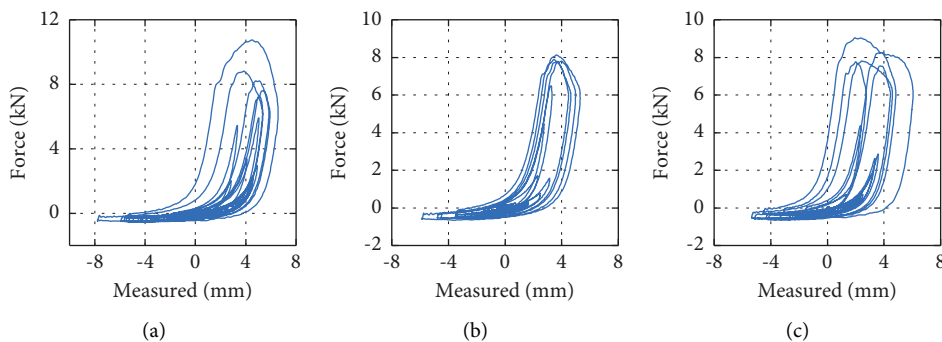

Figure 24: Hysteresis relationship of the damper in the RTHS. (a) El Centro; (b) Kobe; (c) Morgan Hill.

considering the high-frequency dynamic of the system. Furthermore, the proposed method performs the best, indicating the feedback controller contributes to improving the tracking accuracy.

Figure 27 describes the ETHs of the additive error model parameters for the proposed method under three earthquake excitations with a PGA of 0.4 g. The evolutions of the estimated parameters are similar to each other for the considered three excitations. The estimated parameters are almost unchanged at the beginning because the control plant's nonlinearity is very weak. Subsequently, they are updated rapidly in the following 3 s and almost converge to their corresponding constant. Furthermore, the variation ranges for the error model parameters are relatively small for all excitations, namely, from −0.2 to 0.2. The results in Figure 26 also imply that the parameter estimation method
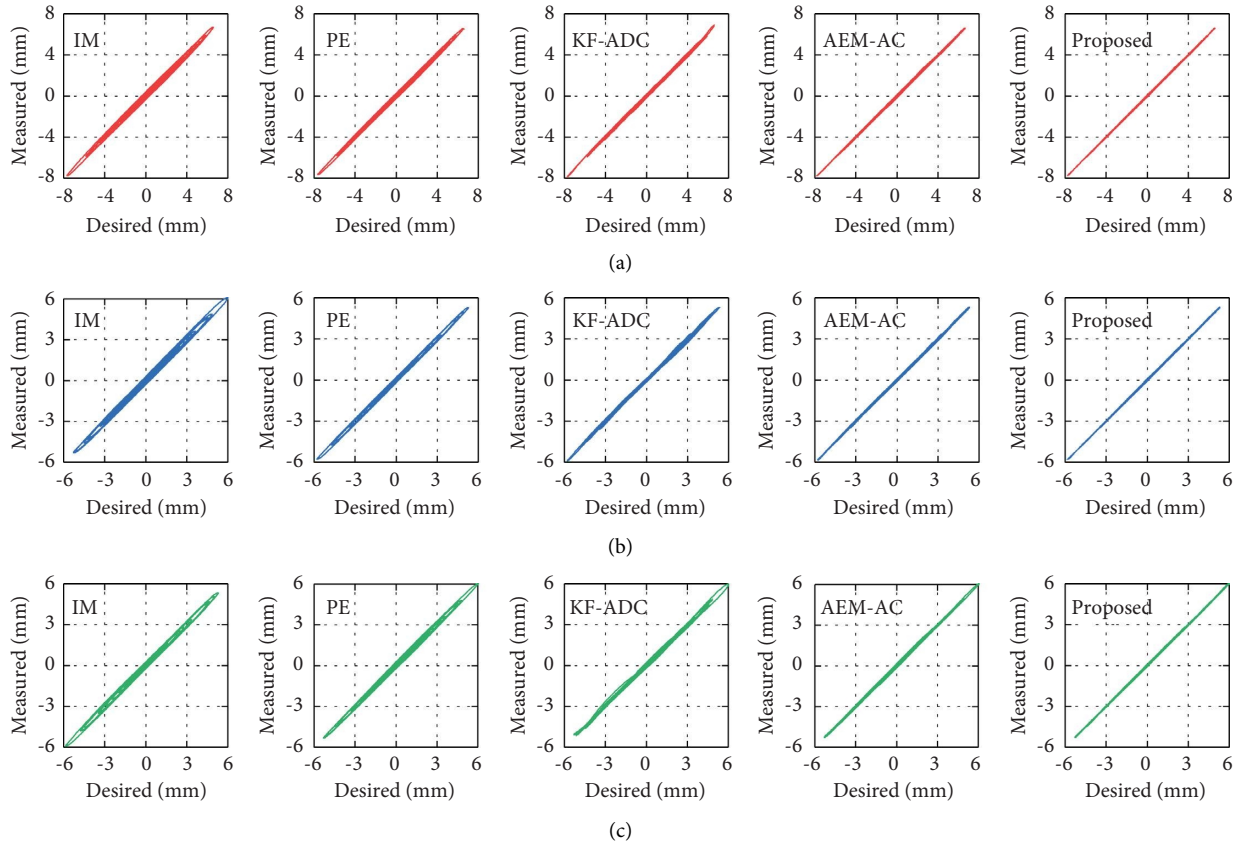
(a)

(b)

(c)

FIGURE 25: D-M displacement plots of comparative methods under three earthquake excitations with PGAs of 0.4*g*. (a) El Centro; (b) Kobe; (c) Morgan Hill.
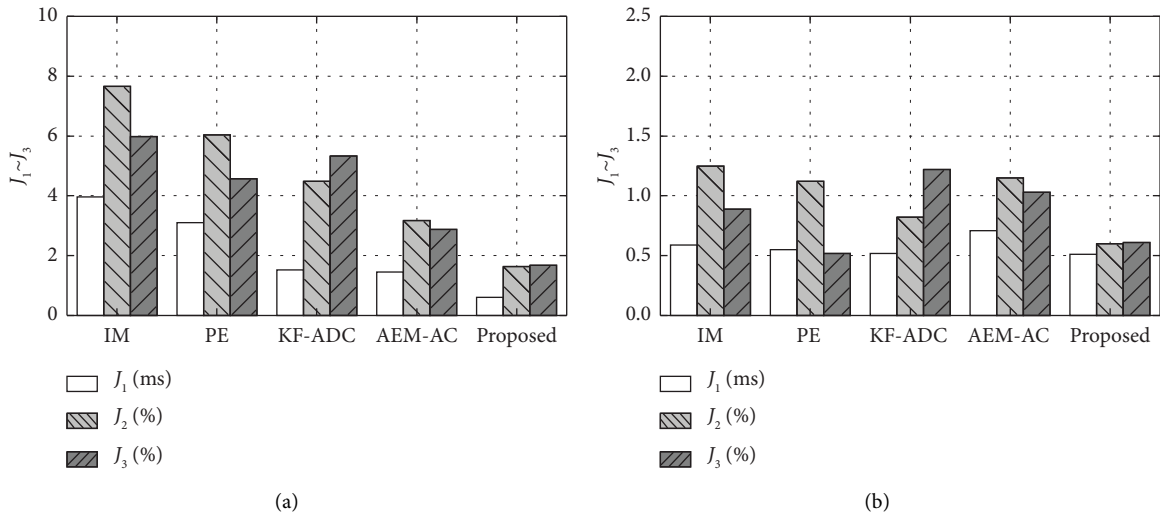

(a)

(b)

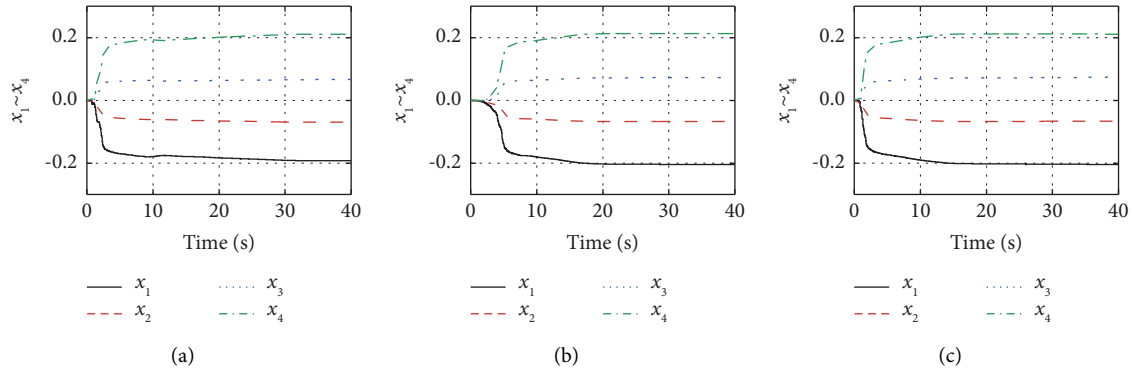FIGURE 26: $J_1 \sim J_3$ in the RTHS. (a) Mean; (b) STD.

FIGURE 27: ETHs of the additive error model parameters. (a) El Centro; (b) Kobe; (c) Morgan Hill.

adopting the Kalman filter can identify the additive error model of the control plant quickly, demonstrating excellent parameter estimation ability.

5. Conclusions

This study proposed a novel adaptive model-based feedforward-feedback control method to deal with the variable time delay in RTHS. Compared with most existing adaptive control methods, it can reduce the dependence on the parameter estimation method as well as the initial parameters of the adaptive control law. The feasibility and effectiveness were examined by the virtual simulations and actual experimental validations, respectively. The major conclusions are as follows.

(1) The formula of the proposed adaptive control method is presented in detail. In this control method, the primary time delay is suppressed by a feedforward controller based on the nominal inverse model of the control plant. To further eliminate the residual time delay, an adaptive controller represented by a difference equation is designed by an additive error model. Finally, a feedback controller is introduced to improve its robustness.

(2) Numerous simulations of RTHS are carried out to verify this method's effectiveness, utilizing a steel frame structure equipped with a damper. The results reveal that the proposed method has a brilliant tracking ability and can effectively improve the accuracy of RTHS. It is necessary to incorporate the additive error model in the proposed method.

(3) Parametric studies are carried out to investigate the critical factors of the proposed method. Results reveal that the initial parameter settings in KF and the additive error model parameter numbers can barely affect the tracking accuracy. The high-order inverse model is unable to enhance the tracking ability of the adaptive control method effectively. The second- or third-order inverse model is recommended to obtain stable and good control performance.

(4) Virtual and actual RTHSs are conducted to validate the performance of the control method. Adaptive control strategies are more accurate than the IM and PE methods, and the proposed control method's errors are smaller than those of the AEM-AC and KF-ADC methods on the whole. Moreover, its standard deviations are the smallest, indicating superb tracking performance and strong robustness in all comparative methods.

Data Availability

The data that support the findings of this study are available from the first or corresponding author upon reasonable request.

Conflicts of Interest

The authors declare that they have no conflicts of interest.

Acknowledgments

References

[1] M. Nakashima, H. Kato, and E. Takaoka, "Development of real-time pseudo dynamic testing," *Earthquake Engineering & Structural Dynamics*, vol. 21, no. 1, pp. 79–92, 1992.

[2] J. E. Carrion and B. J. Spencer, "Real-time hybrid testing using model-based delay compensation," *Smart Structures and Systems*, vol. 4, no. 6, pp. 809–828, 2008.

[3] M. Ahmadizadeh, G. Mosqueda, and A. M. Reinhorn, "Compensation of actuator delay and dynamics for real-time hybrid structural simulation," *Earthquake Engineering & Structural Dynamics*, vol. 37, no. 1, pp. 21–42, 2008.

[4] N. Tsokanas, R. Pastorino, and B. Stojadinović, "Adaptive model predictive control for actuation dynamics compensation in real-time hybrid simulation," *Mechanism and Machine Theory*, vol. 172, Article ID 104817, 2022.

[5] C. Chen, Y. Yang, H. Hou, C. Peng, and W. Xu, "Real-time hybrid simulation with multi-fidelity Co-Kriging for global response prediction under structural uncertainties," *Earthquake Engineering & Structural Dynamics*, vol. 51, no. 11, pp. 2591–2609, 2022.

[6] X. Gao, M. Chen, C. Chen, T. Guo, W. Xu, and K. Cornejo, "Real-time hybrid simulation with Polynomial Chaos NARX Modeling for seismic response evaluation of structures subjected to stochastic ground motions," *Journal of Structural Engineering*, vol. 148, no. 9, 2022.

[7] W. Xu, C. Chen, X. Gao, M. Chen, T. Guo, and C. Peng, "Data-driven nonlinear autoregressive with external input model-based compensation for real-time testing," *Structural Control and Health Monitoring*, vol. 29, no. 12, 2022.

[8] F. Lin, A. Maghareh, S. J. Dyke, and X. Lu, "Experimental implementation of predictive indicators for configuring a real-time hybrid simulation," *Engineering Structures*, vol. 101, pp. 427–438, 2015.

[9] C. Chen, J. M. Ricles, T. M. Marullo, and O. Mercan, "Real-time hybrid testing using the unconditionally stable explicit CR integration algorithm," *Earthquake Engineering & Structural Dynamics*, vol. 38, no. 1, pp. 23–44, 2009.

[10] W. Huang, X. Ning, Y. Ding, and Z. Wang, "A novel actuation dynamics adaptive compensation strategy for real-time hybrid simulation based on unscented kalman filter," *International Journal of Structural Stability and Dynamics*, vol. 23, no. 10, 2022.

[11] X. Gao, N. Castaneda, and S. J. Dyke, "Real time hybrid simulation: from dynamic system, motion control to experimental error: real time hybrid simulation, control, experimental error," *Earthquake Engineering & Structural Dynamics*, vol. 42, no. 6, pp. 815–832, 2013.

[12] A. P. Darby, M. S. Williams, and A. Blakeborough, "Stability and delay compensation for real-time substructure testing," *Journal of Engineering Mechanics*, vol. 128, no. 12, pp. 1276–1284, 2002.

[13] M. I. Wallace, J. Sieber, S. A. Neild, D. J. Wagg, and B. Krauskopf, "Stability analysis of real-time dynamic substructuring using delay differential equation models," *Earthquake Engineering & Structural Dynamics*, vol. 34, no. 15, pp. 1817–1832, 2005.

[14] Y. Tang and H. Qin, "Stability and accuracy analysis of real-time hybrid simulation (RTHS) with incomplete boundary conditions and actuator delay," *International Journal of Structural Stability and Dynamics*, vol. 20, no. 11, Article ID 2050122, 2020.

[15] C. Chen, J. M. Ricles, and T. Guo, "Improved adaptive inverse compensation technique for real-time hybrid simulation," *Journal of Engineering Mechanics*, vol. 138, no. 12, pp. 1432–1446, 2012.

[16] Y. Chae, K. Kazemibidokhti, and J. M. Ricles, "Adaptive time series compensator for delay compensation of servo-hydraulic actuator systems for real-time hybrid simulation," *Earthquake Engineering & Structural Dynamics*, vol. 42, no. 11, pp. 1697–1715, 2013.

[17] P. Chen, C. Chang, B. F. Spencer, and K. Tsai, "Adaptive model-based tracking control for real-time hybrid simulation," *Bulletin of Earthquake Engineering*, vol. 13, no. 6, pp. 1633–1653, 2015.

[18] C. Gálmez and G. Fermandois, "Robust adaptive model-based compensator for the real-time hybrid simulation benchmark," *Structural Control and Health Monitoring*, vol. 29, no. 7, 2022.

[19] A. Najafi and B. F. Spencer Jr, "Adaptive model reference control method for real-time hybrid simulation," *Mechanical Systems and Signal Processing*, vol. 132, pp. 183–193, 2019.

[20] S. Strano and M. Terzo, "Actuator dynamics compensation for real-time hybrid simulation: an adaptive approach by means of a nonlinear estimator," *Nonlinear Dynamics*, vol. 85, no. 4, pp. 2353–2368, 2016.

[21] R. Mirza Hessabi, A. Ashasi-Sorkhabi, and O. Mercan, "A new tracking error-based adaptive controller for servo-hydraulic actuator control," *Journal of Vibration and Control*, vol. 22, no. 12, pp. 2824–2840, 2016.

[22] X. Ning, Z. Wang, C. Wang, and B. Wu, "Adaptive feed-forward and feedback compensation method for real-time hybrid simulation based on a discrete physical testing system model," *Journal of Earthquake Engineering*, vol. 26, no. 8, pp. 3841–3863, 2022.

[23] H. Zhou, D. Xu, X. Shao, X. Ning, and T. Wang, "A robust linear-quadratic-Gaussian controller for the real-time hybrid simulation on a benchmark problem," *Mechanical Systems and Signal Processing*, vol. 133, Article ID 106260, 2019.

[24] Y. Ouyang, W. Shi, J. Shan, and B. F. Spencer, "Backstepping adaptive control for real-time hybrid simulation including servo-hydraulic dynamics," *Mechanical Systems and Signal Processing*, vol. 130, pp. 732–754, 2019.

[25] H. W. Li, A. Maghareh, J. Wilfredo Condori Uribe, H. Montoya, S. J. Dyke, and Z. Xu, "An adaptive sliding mode control system and its application to real-time hybrid simulation," *Structural Control and Health Monitoring*, vol. 29, no. 1, 2022.

[26] Z. Wang, X. Ning, G. Xu, H. Zhou, and B. Wu, "High performance compensation using an adaptive strategy for real-time hybrid simulation," *Mechanical Systems and Signal Processing*, vol. 133, Article ID 106262, 2019.

[27] J. Tao and O. Mercan, "A study on a benchmark control problem for real-time hybrid simulation with a tracking error-based adaptive compensator combined with a supplementary proportional-integral-derivative controller," *Mechanical Systems and Signal Processing*, vol. 134, Article ID 106346, 2019.

[28] D. Xu, H. Zhou, X. Shao, and T. Wang, "Performance study of sliding mode controller with improved adaptive polynomial-based forward prediction," *Mechanical Systems and Signal Processing*, vol. 133, Article ID 106263, 2019.

[29] L. H. Peiris, A. Bartl, J. L. du Bois, and A. Plummer, "Passivity control with adaptive feed-forward filtering for real-time hybrid tests," *IFAC Journal of Systems and Control*, vol. 12, Article ID 100081, 2020.

[30] X. Ning, Z. Wang, and B. Wu, "Kalman filter-based adaptive delay compensation for benchmark problem in real-time hybrid simulation," *Applied Sciences*, vol. 10, no. 20, p. 7101, 2020.

[31] B. D. O. Anderson and A. Dehghani, "Challenges of adaptive control–past, permanent and future," *Annual Reviews in Control*, vol. 32, no. 2, pp. 123–135, 2008.

[32] K. Zhou and J. C. Doyle, *Essentials of Robust Control*, Prentice-Hall, Upper Saddle River, NJ, USA, 1998.

[33] J. Zhao, C. French, C. Shield, and T. Posbergh, "Considerations for the development of real-time dynamic testing using servo-hydraulic actuation," *Earthquake Engineering & Structural Dynamics*, vol. 32, no. 11, pp. 1773–1794, 2003.

[34] J. Zhao, C. Shield, C. French, and T. Posbergh, "Nonlinear system modeling and velocity feedback compensation for

effective force testing," *Journal of Engineering Mechanics*, vol. 131, no. 3, pp. 244–253, 2005.

[35] F. Weber, "Bouc-Wen model-based real-time force tracking scheme for MR dampers," *Smart Materials and Structures*, vol. 22, no. 4, Article ID 045012, 2013.

[36] C. E. Silva, D. Gomez, A. Maghareh, S. J. Dyke, and B. F. Spencer, "Benchmark control problem for real-time hybrid simulation," *Mechanical Systems and Signal Processing*, vol. 135, Article ID 106381, 2020.

[37] T. Horiuchi, M. Inoue, T. Konno, and Y. Namita, "Real-time hybrid experimental system with actuator delay compensation and its application to a piping system with energy absorber," *Earthquake Engineering & Structural Dynamics*, vol. 28, no. 10, pp. 1121–1141, 1999.